Recovering w0 and wa using BAO analysis of dynamical dark energy models in FLAMINGO hydrodynamical simulations

Kortmann, Stan

Recovering w_0 and w_a using BAO analysis of dynamical dark energy models in FLAMINGO hydrodynamical simulations

THESIS

submitted in partial fulfillment of the
requirements for the degree of

MASTER OF SCIENCE
in
PHYSICS

Author :	Stan Kortmann
Student ID :	2334704
Supervisor :	Matthieu Schaller
2^{nd} corrector :	Subodh Patil

Leiden, The Netherlands, February 12, 2026

Recovering w_0 and w_a using BAO analysis of dynamical dark energy models in FLAMINGO hydrodynamical simulations

Stan Kortmann

Instituut-Lorentz, Universiteit Leiden
P.O. Box 9500, 2300 RA Leiden, The Netherlands

February 12, 2026

Abstract

Baryon acoustic oscillations (BAO) provide a probe of cosmic expansion and dark energy. Using FLAMINGO hydrodynamical simulations, we construct DESI-like luminous red galaxy mock catalogues with forward modeled realistic observational effects, measure the anisotropic two point correlation function across redshifts, and fit linear theory BAO templates to constrain Chevallier–Polarski–Linder parameters w_0 and w_a of dynamical dark energy equation of state. We validate the pipeline by recovering fiducial cosmology and testing departures from ΛCDM, finding the BAO scale robust to baryonic effects and galaxy selection, with residual systematics subdominant to statistical uncertainties, yielding w_0–w_a constraints consistent with DESI expectations.

Contents

Version of February 12, 2026– Created February 12, 2026 - 20:24

Chapter 1

Introduction

1.1 Cosmological context

Large scale galaxy redshift surveys probe the expansion history and the growth of cosmic structure of the universe. In the standard cosmological paradigm, structures form from small primordial density perturbations through gravitational instability, leading to the observed web-like distribution of galaxies on large scales that we can see now. Connecting these late time observables to early universe physics is a central goal of modern cosmology. Baryon acoustic oscillations (BAO) is one of the processes that emerge in the early universe and its effect can still be measured in the later stages of the universe.

1.2 Physical origin of baryon acoustic oscillations

Baryon acoustic oscillations originate from the evolution of primordial density perturbations in the early universe, when baryons and photons formed a tightly coupled plasma through Thomson scattering. In this regime, perturbations evolved under the competing effects of gravitational collapse and radiation pressure. Overdensities in the plasma consisting of photons and baryons drove outward propagating sound waves. Dark matter perturbations evolved collisionless and provided a near constant gravitational potential at the overdensities from where the plasma sound waves are propagating.[1][2]

The propagation of these acoustic waves continued until recombination, when electrons and protons combined to form neutral hydrogen and the photon mean free path increased dramatically. Following this decoupling, photon pressure ceased to influence baryons, freezing in a characteristic comoving scale corresponding to the maximum distance traveled by sound waves in the primordial plasma. This scale, known as the sound horizon at the baryon drag epoch, is imprinted in the baryon distribution, transferred to the total matter field and finally in the galaxy distribution that we can observe today.[3]

1.3 BAO as a standard ruler

The sound horizon scale provides a standard ruler whose physical length can be predicted from early universe physics. It depends primarily on the physical baryon density, the matter density, and the radiation content of the universe, all of which are tightly constrained by observations of the cosmic microwave background (CMB). [4]

Although non-linear gravitational evolution, galaxy bias, and redshift-space distortions modify the amplitude and shape of the BAO feature, these effects do not significantly shift its position and thus the rulers length as to be proven in this thesis.[5] As a result, this ruler can be used to assert the distance between observer and the galaxy pair via parallax.

1.4 BAO in galaxy surveys

In observational data, BAO appear as a series of oscillations in the galaxy power spectrum and as a broad peak in the two point correlation function at a comoving separation of approximately 150 Mpc.[6] Galaxies trace the underlying matter distribution in a biased manner, but on sufficiently large scales this bias is approximately linear and does not affect the BAO scale length as imprinted in the matter power spectrum.[7]

Modern spectroscopic surveys are designed to optimize the measurement of BAO across a wide range of redshifts. In particular, luminous red galaxies (LRGs) are highly biased tracers that can be observed with accurate redshifts over large cosmological volumes, making them well suited for BAO analyses. The Dark Energy Spectroscopic Instrument (DESI) is currently measuring BAO with high statistical precision using multiple galaxy

and quasar samples at different redshifts and recently released data that shows our current limited understanding of dark energy might not be true.[8–10]

1.5 Simulations and realistic mock catalogs

As statistical uncertainties decrease, systematic effects associated with non-linear structure formation, redshift space distortions, and survey selection functions become increasingly important. Numerical simulations provide a tool for studying these effects in a controlled setting and for connecting theoretical predictions to observational measurements.

While dark–matter–only simulations capture the dominant gravitational dynamics on large scales, hydrodynamical simulations include baryonic processes such as gas cooling, star formation, and feedback processes, which can influence galaxy bias and clustering statistics. Forward modeling galaxy surveys within such simulations (by applying realistic selection criteria and observational effects such as redshift measurement errors) is therefore critical for interpreting observational BAO measurements and for validating their outcomes.

1.6 Aim and structure

The aim of this thesis is to study the imprint of baryon acoustic oscillations in simulated galaxy populations and to assess the impact of realistic survey selections on BAO measurements. Using the FLAMINGO hydrodynamical simulations[11], mock galaxy catalogs are constructed to emulate DESI like luminous red galaxy samples, and their clustering properties are analysed. After analysis a conclusion can be made on whether the DESI results are reproducible in the FLAMINGO simulation suite and if we will have to rethink our understanding of how dark energy behaves.

Version of February 12, 2026– Created February 12, 2026 - 20:24

Chapter 2

Theoretical background

2.1 Derivation of the BAO length scale from FLRW background and fluid dynamics

Baryon acoustic oscillations (BAO) originate from acoustic waves in the photon–baryon plasma prior to recombination. The BAO length scale is set by the comoving distance a sound wave can travel from very early in the universe up to the end of photon–baryon coupling (the baryon drag epoch). This distance is the sound horizon at drag, $r_s(z_d)$, which sets the characteristic spacing of oscillatory features in the matter power spectrum and ultimately in the galaxy distribution.[2–4, 12]

In this section $r_s(z_d)$ will be derived by using perturbations of the FLRW metric and fluid equations.

2.1.1 Homogeneous background: FLRW metric, equations of state, and expansion history

We begin with a homogeneous and isotropic Friedmann–Lemaître–Robertson–Walker (FLRW) spacetime,

$$ds^2 = -dt^2 + a^2(t)\left[\frac{dr^2}{1-Kr^2} + r^2(d\theta^2 + \sin^2\theta\, d\phi^2)\right], \qquad (2.1)$$

where $a(t)$ is the scale factor and K is the spatial curvature constant. [13]

Each component i is modeled as a perfect fluid with equation of state. $i = c$ is cold dark matter, $i = b$ is baryonic matter, $i = \gamma$ are photons, $i = K$ is curvature, $i = \nu$ is the combination of all relativistic neutrino's. and $i = \Lambda$ is non–dynamical dark energy.

$$p_i = w_i \rho_i, \tag{2.2}$$

with

and curvature can be represented as an effective component with $w_K = -1/3$ in the Friedmann equation.

Energy–momentum conservation for each non-interacting background component implies the continuity equation [13]

$$\dot{\rho}_i + 3H(1 + w_i)\rho_i = 0, \tag{2.3}$$

whose solution is

$$\rho_i(a) = \rho_{i,0}\, a^{-3(1+w_i)}. \tag{2.4}$$

Defining present-day (note the subscript 0) density parameters

$$\Omega_{i,0} \equiv \frac{\rho_{i,0}}{\rho_{crit,0}}, \qquad \rho_{crit,0} \equiv \frac{3H_0^2}{8\pi G}, \tag{2.5}$$

the Hubble expansion rate becomes

$$H(a) = H_0\, E(a), \qquad E(a) = \sqrt{\Omega_{r,0}a^{-4} + \Omega_{m,0}a^{-3} + \Omega_{K,0}a^{-2} + \Omega_{\Lambda,0}}, \tag{2.6}$$

where $\Omega_{m,0} = \Omega_{b,0} + \Omega_{c,0}$ and $\Omega_{r,0} = \Omega_{\gamma,0} + \Omega_{\nu,0}$ includes photons plus relativistic neutrinos at early times. [4, 13, 14]

2.1.2 The photon–baryon oscillator

Before recombination at $z \approx 1100$, Thomson scattering couples photons to baryons. In this tight-coupling regime the photon and baryon velocities are nearly.

$$\theta_\gamma \simeq \theta_b \equiv \theta_{\gamma b}. \tag{2.7}$$

Define the baryon-loading parameter

$$R(\eta) \equiv \frac{3\bar{\rho}_b}{4\bar{\rho}_\gamma}. \tag{2.8}$$

Because $\rho_b \propto a^{-3}$ and $\rho_\gamma \propto a^{-4}$, we have $R(a) \propto a$ and, explicitly,

$$R(a) = \frac{3}{4}\frac{\Omega_{b,0}}{\Omega_{\gamma,0}}\, a. \tag{2.9}$$

In tight coupling, the photon–baryon system behaves as an effective single fluid with outward pressure dominated by photons and inward inertia from baryons.[3, 12] You can see how the density of either one of them effects the effective sound speed in Eq. 2.10

$$c_s^2(a) \equiv \frac{\delta p}{\delta \rho} \simeq \frac{1}{3(1+R(a))}. \tag{2.10}$$

Deriving the oscillator A compact way to see the acoustic nature is to combine the photon continuity and Euler equations with baryon inertia included via R. One obtains an oscillator equation for the photon–baryon density perturbation

$$\delta''_{\gamma b} + \frac{R'}{1+R}\,\mathcal{H}\,\delta'_{\gamma b} + c_s^2 k^2\,\delta_{\gamma b} \simeq -k^2\Psi \tag{2.11}$$

which is a forced harmonic oscillator with (time-dependent) frequency $k\,c_s$ and where Ψ is the perturbation field which has been introduced on top of the standard FLRW field. [2, 12, 14]

Version of February 12, 2026– Created February 12, 2026 - 20:24

If c_s and R vary slowly over one oscillation ($R' \approx 0$), the homogeneous solution is approximately

$$\delta_{\gamma b}(k, \eta) \propto \cos[k\, r_s(\eta)] \tag{2.12}$$

where the phase is set by the sound horizon $r_s(\eta)$

$$r_s(\eta) \equiv \int_0^\eta c_s(\tilde{\eta})\, d\tilde{\eta}. \tag{2.13}$$

So at a certain time in the early universe η, acoustic waves can propagate between the a fixed overdensity at $r = 0$ and the sound horizon at $r = r_s$ in configuration space. This means a certain k-mode has to fullfill the following equation to be oscillating:

$$\frac{2\pi}{k} \leq r_s(\eta) \tag{2.14}$$

Sound waves from overdensities attributed to a certain k-mode will first feel the sound wavefront from their nearest neighbours $r = \frac{2\pi}{k}$ when Eq. 2.14 is first true at a certain η. Afterwards this k mode is activated and in Fourier space can be seen oscillating in time from that point onwards. This oscillation frequency for a set k-mode is time dependent (because the propagation speed of the fluid c_s is time dependent as seen in Eq. 2.12 and 2.13). Higher value k-modes with a respective lower wavelength separation (which enter the sound horizon at an earlier time in the universe) in configurations space will have oscillated longer than lower value k-modes.

2.1.3 The drag epoch and freeze-out of the BAO ruler

As the universe cools, recombination reduces the free-electron density and Thomson scattering becomes ineffective. Photons decouple and free-stream: baryons cease to be tightly driven by photon pressure and stop moving outwards with respect to the initial overdensity center. The relevant time for imprinting the BAO ruler in the matter distribution is the baryon drag epoch (often denoted z_d), when drag from baryon–photon interactions effectively ends.[3, 4, 12] In practice, z_d depends on the ionisation history ($\chi_e(z)$, the free electron fraction, dictates the effectiveness of Thomson scattering inside the photon–baryon fluid) and is usually computed numerically (e.g. in `CAMB`[15]). [3, 4, 12]

2.1.4 Sound horizon at drag

The sound horizon is defined as

$$r_s(\eta_d) = \int_0^{\eta_d} c_s(\eta)\, d\eta. \tag{2.15}$$

Changing variables to scale factor a and using $d\eta = da/(a^2 H(a))$ gives

$$r_s(a_d) = \int_0^{a_d} \frac{c_s(a)}{a^2 H(a)}\, da = \frac{1}{H_0} \int_0^{a_d} \frac{c_s(a)}{a^2 E(a)}\, da, \tag{2.16}$$

where $E(a)$ is given by Eq. (2.6).
Using Eqs. 2.9 and 2.10, the integrand is fully specified by $\Omega_{b,0}$, $\Omega_{\gamma,0}$, and the background expansion through $(\Omega_{r,0}, \Omega_{m,0}, \Omega_{K,0}, \Omega_{\Lambda,0})$:

$$c_s(a) = \frac{1}{\sqrt{3\left[1 + \frac{3}{4}\frac{\Omega_{b,0}}{\Omega_{\gamma,0}} a\right]}}. \tag{2.17}$$

Thus the sound horizon r_s in the matter power spectrum is determined by early-time particle physics (through $c_s(a)$) and by the expansion rate (through $E(a)$) at the drag epoch a_d when the photon pressure component ceases to exist. [3, 4, 12] The oscillations will stop and the phase of the oscillations imprinted in the matter power spectrum for values of k that entered the sound horizon before the drag epoch.

2.1.5 Acoustic feature in $P(k)$

The oscillatory dependence $\cos(kr_s)$ implies extrema (peaks and troughs) when

$$k_n \simeq \frac{n\pi}{r_s(z_d)} \qquad (n = 1, 2, 3, \ldots), \tag{2.18}$$

so the fundamental BAO scale in Fourier space is

$$\Delta k_{\mathrm{BAO}} \simeq \frac{\pi}{r_s(z_d)}. \tag{2.19}$$

In the matter power spectrum the BAO appear as a series of wiggles with characteristic spacing $\Delta k \simeq \pi/r_s \approx 0.03\, h/Mpc$ as seen in figure 2.1.

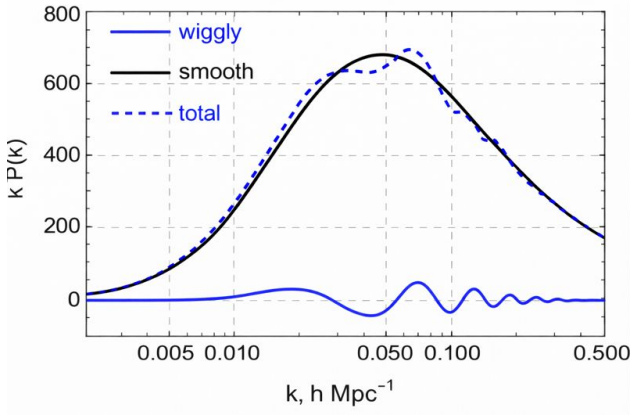

Figure 2.1: *Illustrative plot showing the smooth (CDM) and wiggly (Baryons) contributions to the total matter power spectrum function of the universe.[7]*

2.2 Galaxy two-point correlation function

The baryon acoustic oscillation feature appears in two equivalent but complementary representations of large-scale structure: as oscillations in the matter power spectrum $P(k)$ and as a localized excess in the real-space two-point correlation function $\xi(r)$. The connection between these two descriptions follows directly from Fourier transformations.

For a statistically homogeneous and isotropic density field, the two-point correlation function is defined as

$$\xi(r) \equiv \langle \delta(\boldsymbol{x})\, \delta(\boldsymbol{x}+\boldsymbol{r}) \rangle, \tag{2.20}$$

and is related to the matter power spectrum via [7]

$$\xi(r) = \frac{1}{2\pi^2} \int_0^\infty dk\, k^2\, P(k)\, \frac{\sin(kr)}{kr}. \tag{2.21}$$

As discussed previously, the linear matter power spectrum can be decomposed into a smooth and an oscillatory component,

$$P(k) = P_{\mathrm{s}}(k) + P_{\mathrm{w}}(k), \tag{2.22}$$

where $P_{\mathrm{s}}(k)$ is a broadband contribution and the BAO signal is contained in the "wiggly" component $P_{\mathrm{w}}(k)$. To leading order, the oscillatory part may be approximated as

$$P_{\mathrm{w}}(k) \simeq A(k)\, \sin\big(kr_s + \varphi\big), \tag{2.23}$$

with r_s the sound horizon at the baryon drag epoch and φ a weakly scale-dependent phase.[3, 16]

Substituting Eq. (2.23) into Eq. (2.21) shows that the oscillatory behavior in Fourier space does not map to oscillations in configuration space. Instead, the product of sine functions in the integrand leads to constructive interference when the separation r is close to the sound horizon,

$$\xi_{\mathrm{w}}(r) \;\propto\; \int dk\, k^2\, \sin(kr_s)\, \frac{\sin(kr)}{kr}, \tag{2.24}$$

and destructive interference away from this scale. The net result is a single, localized enhancement in the two-point correlation function centered at

$$r \simeq r_s(z_d). \tag{2.25}$$

This feature admits a particularly intuitive physical interpretation. An initial overdensity in the early universe launches a spherical acoustic wave in the photon–baryon plasma. By the baryon drag epoch, baryons have accumulated both at the origin and on a thin shell of radius r_s as can be seen in figure 2.2.

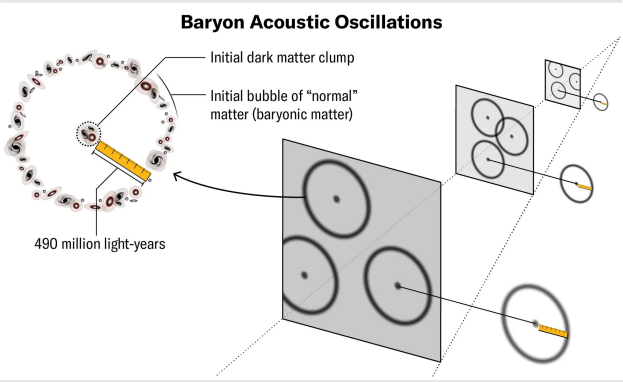

Figure 2.2: *Illustration [17] showing the imprinted rings of baryonic matter after the drag epoch around a local overdensity.*

After recombination, baryons fall back into dark matter potential wells, but the characteristic separation imprinted by this shell survives gravitational evolution as not all of the baryons fall into the potential wells. At late times, galaxy pairs therefore exhibit an enhanced probability of being separated by a distance close to r_s, producing the BAO bump in $\xi(r)$.[1, 3] A timelapse of how the BAO is formed can be seen on the next page and is copied straight out of the following paper [18] (Figure itself is from [19]).

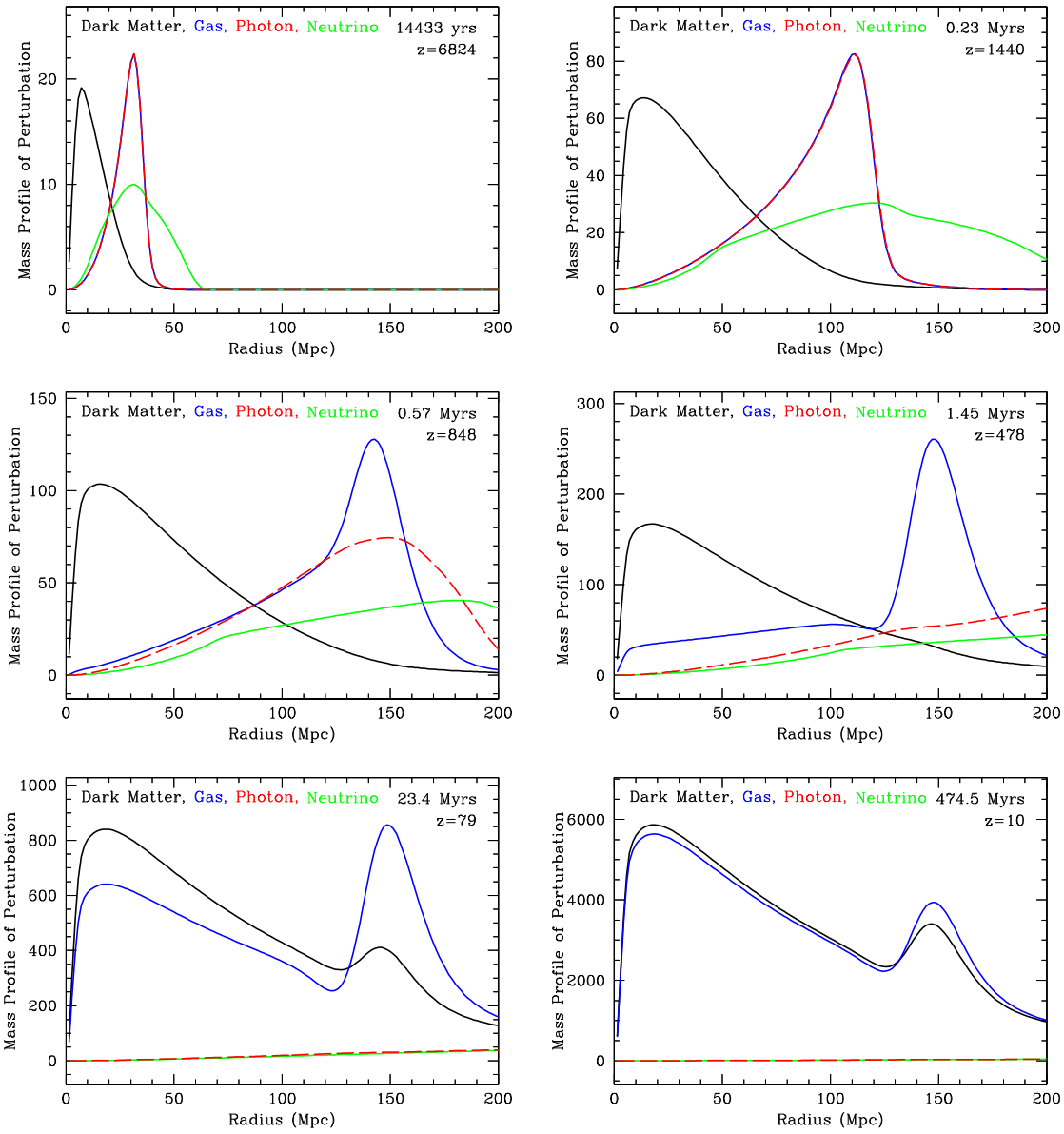

Fig. 1.10. **Snapshots of an evolving spherical density perturbation** – the radial mass profile as a function of comoving radius for an initially point-like overdensity located at the origin. The perturbations in the dark matter (black curve), baryons (blue curve), photons (red) and neutrinos (green) evolve from early times ($z = 6824$, top left) to long after decoupling ($z = 10$, bottom right). Initially the density perturbation propagates through the photons and baryons as a single pulse (top left-hand panel). The drag of the photons and baryons on the dark matter is visible in the top right panel; the dark matter only interacts gravitationally and therefore its perturbation lags behind that of the tightly coupled plasma. During recombination, however, the photons start to "leak" away from the baryons (middle left panel); and once recombination is complete ($z = 470$, middle right) the photons freely steam away leaving only a density perturbation in the baryons around 150Mpc, and a dark matter perturbation near the origin. In the bottom two panels we see the how the gravitational interaction between the dark matter and the baryons affects the peak: dark matter pulls the baryons to the peak in the density near zero radius, while the baryons continue to drag the dark matter overdensity towards the 150Mpc peak (bottom left), finally yielding a peak in the radial mass profile of the dark matter at the scale set by the distance the baryon-photon acoustic wave could have travelled in the time before recoupling. Figure taken from Eisenstein *et al.* (50).

2.2.1 Alcock–Paczyński effect

Galaxy redshift surveys measure angular positions and redshifts rather than comoving distances. To construct a three-dimensional map of the galaxy distribution, observed redshifts are converted into comoving distances using the radial comoving distance

$$D_C(z) \equiv \chi(z) = \int_0^z \frac{c\,dz'}{H(z')}, \tag{2.26}$$

(for a spatially flat FLRW model. Curvature generalizations can be introduced via $D_M(z) = S_k[\chi(z)]$ which is shown in the Methods chapter). Combined with the angular coordinates, this mapping assigns each galaxy a position in comoving space, from which pairwise separations are computed and the (weighted) two-point correlation function is measured.

Transverse separations: $s_\perp$. Consider two galaxies at (approximately) the same redshift z but separated by a small angular distance $\Delta\theta$ on the sky (so their separation is mainly perpendicular to the line of sight). At fixed z, the comoving distance to the shell is $D_M(z)$, so the transverse comoving separation is

$$s_\perp \;\simeq\; D_M(z)\,\Delta\theta. \tag{2.27}$$

In this case, both galaxies lie on (nearly) the same constant-z surface, so $H(z)$ only enters implicitly through the single-number mapping $z \mapsto D_M(z)$ in Eq. (2.26). In particular, for a given pair at redshift z, $H(z)$ is not sampled along the pair separation; it is only used to convert the observed redshift to the distance $D_M(z)$.

Radial separations: $s_\parallel$. Now consider a pair with negligible angular separation (same sky position to good approximation) but with different redshifts z_1 and z_2 (so the separation is mainly along the line of sight). Their comoving radial coordinates are $\chi(z_1)$ and $\chi(z_2)$, hence the line-of-sight comoving separation is

$$s_\parallel \;\simeq\; |\chi(z_1) - \chi(z_2)| \;=\; \left| \int_{z_2}^{z_1} \frac{c\,dz'}{H(z')} \right|. \tag{2.28}$$

If the pair is close in redshift, define $z \equiv (z_1 + z_2)/2$ and $\Delta z \equiv z_1 - z_2$ with $|\Delta z| \ll 1$. Then $H(z')$ varies little over the interval, and the integral can be approximated by evaluating H at the midpoint:

$$s_\parallel \;\simeq\; \frac{c\,|\Delta z|}{H(z)}. \tag{2.29}$$

Version of February 12, 2026– Created February 12, 2026 - 20:24

This makes the distinction clear: transverse separations depend on $D_M(z)$ (a distance inferred from integrating $1/H$ from 0 to z), while radial separations depend directly on the local inverse Hubble rate $1/H(z)$ through the differential relation $d\chi/dz = c/H(z)$.

If the cosmological model used to convert redshifts to comoving distances differs from the true cosmology, the inferred separations are distorted anisotropically. In particular, the BAO scale is shifted by different amounts for separations parallel and perpendicular to the line of sight. This geometric distortion is known as the Alcock–Paczyński (AP) effect.[20]

The AP effect manifests itself most clearly in the two-dimensional two-point correlation function $\xi(s, \mu)$, where s is the distance between 2 galaxies and $\mu = cos(\theta)$ where θ denotes angle between the line of sight and the vector between the 2 galaxies. In the correct cosmology, the BAO feature appears approximately isotropic, meaning that $\xi(s, \mu) \approx \xi(s)$. If the wrong cosmology is inferred, the BAO signal will appear at different separation s depending on the orientation in respect to the line of sight μ. Thus the spherical shell seen in figure 2.2 can be distorted depending on the value of μ as is schematically drawn in figure 2.3. We use $\alpha_\perp$ and $\alpha_\parallel$ which are defined in Eq. 2.30. In a correct cosmology $s_\perp = s_\parallel$ with $\alpha_\perp = \alpha_\parallel = 1$.

$$\begin{aligned} \alpha_\perp &= \frac{s_\perp}{s_{\perp,fiducial}} = \frac{s(\mu = 1)}{s_{fiducial}(\mu = 1)} \\ \alpha_\parallel &= \frac{s_\parallel}{s_{\parallel,fiducial}} = \frac{s(\mu = 0)}{s_{fiducial}(\mu = 0)} \end{aligned} \tag{2.30}$$

By measuring the BAO signal as a function of orientation relative to the line of sight, one can therefore constrain the cosmological parameters governing the expansion history. In practice, this information is often extracted either from the anisotropic two-point correlation function or from its multipole moments, with the AP effect providing sensitivity to the geometry of the universe in addition to the overall BAO scale. [3, 21]

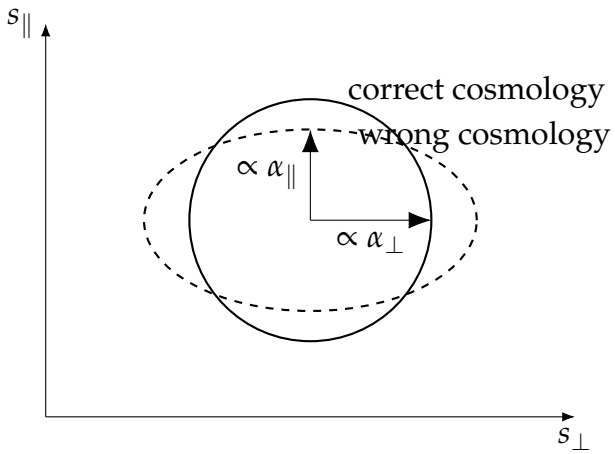

Figure 2.3: *Schematic illustration of the Alcock–Paczynski effect on anisotropic BAO. In the correct cosmology the BAO feature is approximately isotropic (solid circle), while an incorrect mapping from redshift to distance distorts the BAO ring into an ellipse (dashed).*

2.3 Dark energy models

The observed late-time accelerated expansion of the universe is commonly attributed to a dark energy (DE) component with negative pressure. Within a homogeneous and isotropic FLRW background, dark energy can be characterised by its equation-of-state parameter rewriting Eq. 2.2 into Eq. 2.31:

$$w \equiv \frac{p_{\mathrm{DE}}}{\rho_{\mathrm{DE}}}, \tag{2.31}$$

where p_{DE} and ρ_{DE} denote the pressure and energy density of the dark energy component, respectively. Different physical models of dark energy correspond to distinct values and possible time evolution of w, which can be broadly classified into three categories: a cosmological constant, quintessence models, and phantom models.

2.3.1 Cosmological constant

The simplest dark energy model is a cosmological constant Λ, corresponding to a constant equation-of-state parameter

$$w = -1.$$

In this case, the dark energy density remains constant in time, as can be seen from Eq. 2.4, $\rho_\Lambda = \text{const}$. The associated negative pressure, $p_\Lambda = -\rho_\Lambda$, leads to a repulsive gravitational effect in general relativity and drives the late time accelerated expansion of the universe.

Physically, a cosmological constant can be interpreted as a constant vacuum energy density permeating spacetime. When included in the Einstein field equations, it modifies the Friedmann equations through the term Ω_Λ that dominates the cosmic energy budget at late times seen in Eq. 2.6, naturally producing acceleration once the matter density Ω_m has sufficiently diluted.

Version of February 12, 2026– Created February 12, 2026 - 20:24

2.3.2 Quintessence models $(w > -1)$

Quintessence models describe dark energy as a minimally coupled scalar field evolving in a potential $V(\phi)$. [22] In these models, the equation-of-state parameter satisfies

$$-1 < w < 1$$

The energy density of the quintessence field decreases as the universe expands, leading to a dynamical dark energy component whose influence becomes dominant later than the cosmological constant and phantom dark energy models. It also causes the universe to expand at a slower rate than the other 2 models.

2.3.3 Phantom dark energy ($w < -1$)

Phantom dark energy models are characterised by an equation-of-state parameter

$$w < -1$$

corresponding to an energy density that increases with cosmic time as seen in Eq. 2.4. Such behaviour can give rise to exotic future scenarios, including a "Big Rip" singularity, in which bound structures are eventually torn apart. [23]

Although phantom dark energy is not excluded by current observations, realising $w < -1$ typically requires fields with negative kinetic energy, which may lead to instabilities at the quantum level. For this reason, phantom models are often regarded as effective descriptions rather than fundamental theories.

Version of February 12, 2026– Created February 12, 2026 - 20:24

2.3.4 Dynamical dark energy and regime crossing

More generally, dark energy may be dynamical, with an equation-of-state parameter that evolves with cosmic time and transitions between the regimes described above. In such scenarios, the effective equation of state may evolve from quintessence-like behaviour ($w > -1$) to phantom-like behaviour ($w < -1$), or vice versa, crossing the so-called "phantom divide" at $w = -1$.

While a strict crossing of $w = -1$ cannot occur in simple single-field quintessence models, it may arise in more complex scenarios involving multiple scalar fields, non-minimal couplings, or modifications of gravity. [24]

Version of February 12, 2026– Created February 12, 2026 - 20:24

Chapter 3

Method

3.1 Constraining Dark Energy with BAO Measurements

To constrain the time evolution of the dark energy equation of state, a common approach is to employ a parametric form such as the Chevallier–Polarski–Linder (CPL) parametrization. In this framework, the equation of state is written as a function of the scale factor a (or equivalently redshift z) as

$$w(a) = w_0 + w_a(1-a) = w_0 + w_a \frac{z(a)}{1+z(a)}, \tag{3.1}$$

where w_0 denotes the present-day value of the dark energy equation of state and w_a characterizes its time evolution.
Substituting Eq. 3.1 into the dark energy continuity equation (Eqs. 2.4 and 2.2) yields a redshift-dependent dark energy density,

$$\rho_{\mathrm{DE}}(z) = \rho_{\mathrm{DE},0}\,(1+z)^{3(1+w_0+w_a)} \exp\left[-3w_a \frac{z}{1+z}\right]. \tag{3.2}$$

The Hubble expansion rate for a non-flat universe then takes the form

$$\begin{aligned} H^2(z) = H_0^2\Big[&\Omega_{\mathrm{m}}(1+z)^3 + \Omega_{\mathrm{r}}(1+z)^4 + \Omega_k(1+z)^2 \\ &+ \Omega_{\mathrm{DE}}(1+z)^{3(1+w_0+w_a)} \exp\left(-3w_a \frac{z}{1+z}\right)\Big]. \end{aligned} \tag{3.3}$$

The CPL parameters (w_0, w_a) therefore enter directly into the expansion history through $H(z)$, modifying cosmological distance measures used in baryon acoustic oscillation (BAO) analyses.

Single measurements of the BAO scale at a particular redshift are primarily sensitive to a specific combination of w_0 and w_a, leading to degeneracy directions in the w_0–w_a parameter plane. You are in fact only constraining $w(z)$ for

$$z - \Delta z \leq z \leq z + \Delta z$$

in the data analysis of a single redshift bin with binwidth Δz . Combining BAO measurements across multiple redshift bins decreases the degeneracy because each redshift bin probes a different weighting of the equation-of-state evolution (3.4) due to the different z and thus $w(z)$, thereby tightening the joint constraints on both parameters.[5, 25, 26]
This behavior can be understood by defining an effective equation of state at redshift z_i,

$$w(z_i) = w_0 + w_a \frac{z_i}{1 + z_i}, \tag{3.4}$$

which represents the linear combination of CPL parameters most directly constrained by distance measurements at that redshift. As z_i varies, the corresponding degeneracy direction in the (w_0, w_a) plane rotates, enabling multi-bin BAO analyses in large spectroscopic surveys to significantly improve constraints on the time evolution of dark energy.
When combining measurements from multiple redshift bins, the joint likelihood is formally given by

$$\mathcal{L}_{\text{joint}}(w_0, w_a) = P(\mathbf{d}_{z_1}, \mathbf{d}_{z_2}, \ldots, \mathbf{d}_{z_N} \mid w_0, w_a)\,, \tag{3.5}$$

with d_{z_i} being the data vectors in the different redshift bins.
When assuming full gaussian likelihoods we expect the following full joint likelihood

$$\mathcal{L}_{\text{joint}}(w_0, w_a) = \frac{1}{\sqrt{(2\pi)^k \det \mathbf{C}}} \times \exp\left[-\frac{1}{2}\left(\mathbf{D} - \mathbf{M}(w_0, w_a)\right)^{\mathrm{T}} \mathbf{C}^{-1} \left(\mathbf{D} - \mathbf{M}(w_0, w_a)\right)\right], \tag{3.6}$$

$$\mathbf{C} = \begin{pmatrix} \mathbf{C}_{11} & \mathbf{C}_{12} & \cdots & \mathbf{C}_{1N} \\ \mathbf{C}_{21} & \mathbf{C}_{22} & \cdots & \mathbf{C}_{2N} \\ \vdots & \vdots & \ddots & \vdots \\ \mathbf{C}_{N1} & \mathbf{C}_{N2} & \cdots & \mathbf{C}_{NN} \end{pmatrix}, \tag{3.7}$$

Version of February 12, 2026– Created February 12, 2026 - 20:24

$\mathbf{C}$ is the full covariance matrix. Redshift bins i and j are independent whenever $\mathbf{C}_{ij} = 0$. $\mathbf{M}(w_0, w_a)$ Is the vector that contains the expected data vector assuming our $w_0 w_a CDM$ model. Finally, $\mathbf{D}$ contains the data measurement of the BAO signal in the 2PCF.

In observational analyses, the full covariance between redshift bins is typically estimated from mock catalogs or analytical models and incorporated into the joint likelihood to account for correlations between bins.[5, 26] This ensures that the uncertainties are not artificially decreased when combining bins that share large-scale modes and thus are not statistically independent.

In simulation-based studies, like FLAMINGO, using the same initial density field, it is common to approximate snapshots at different redshifts as statistically independent, particularly when the bins are widely separated. Under this approximation, the joint likelihood reduces to the simple product in equation (3.8).[27] However, this is only an approximation:

$$\mathcal{L}_{\text{joint}}(w_0, w_a) = \mathcal{L}_{z_1}(w_0, w_a) \times \mathcal{L}_{z_2}(w_0, w_a) \times \cdots , \tag{3.8}$$

or, equivalently in terms of χ^2,

$$\chi^2_{\text{joint}}(w_0, w_a) = \sum_i \chi^2_{z_i}(w_0, w_a). \tag{3.9}$$

The large-scale density field modes are coherent across snapshots, leading to significant covariance between BAO measurements at different redshifts. Modes that contribute to the BAO feature at one redshift also influence the BAO in other snapshots. Neglecting this correlation underestimates uncertainties and artificially tightens constraints in the (w_0, w_a) plane. Proper treatment therefore requires estimating the cross-covariance between redshift bins and incorporating it into a joint likelihood or χ^2 analysis, as is standard in observational combined analyses. [5, 28]

Finally, combining BAO measurements with other cosmological probes, such as supernovae or cosmic microwave background data, further breaks degeneracies and improves the overall figure of merit for dark energy parameters. [27]

Version of February 12, 2026– Created February 12, 2026 - 20:24

3.2 Methodology

3.2.1 Pipeline overview

We construct DESI-like luminous red galaxy (LRG) mock observations from the FLAMINGO simulations, measure the two-point correlation function (2PCF), and infer cosmological constraints by comparing the measured BAO scale to theoretical templates under varying cosmological assumptions. The pipeline has three stages as seen in the flow chart in Fig. 3.1:

1) **mock survey construction and target selection**

2) **cosmology-dependent remapping and 2PCF computation (MPI-parallel)**

3) **likelihood combination and posterior inference**

Version of February 12, 2026– Created February 12, 2026 - 20:24

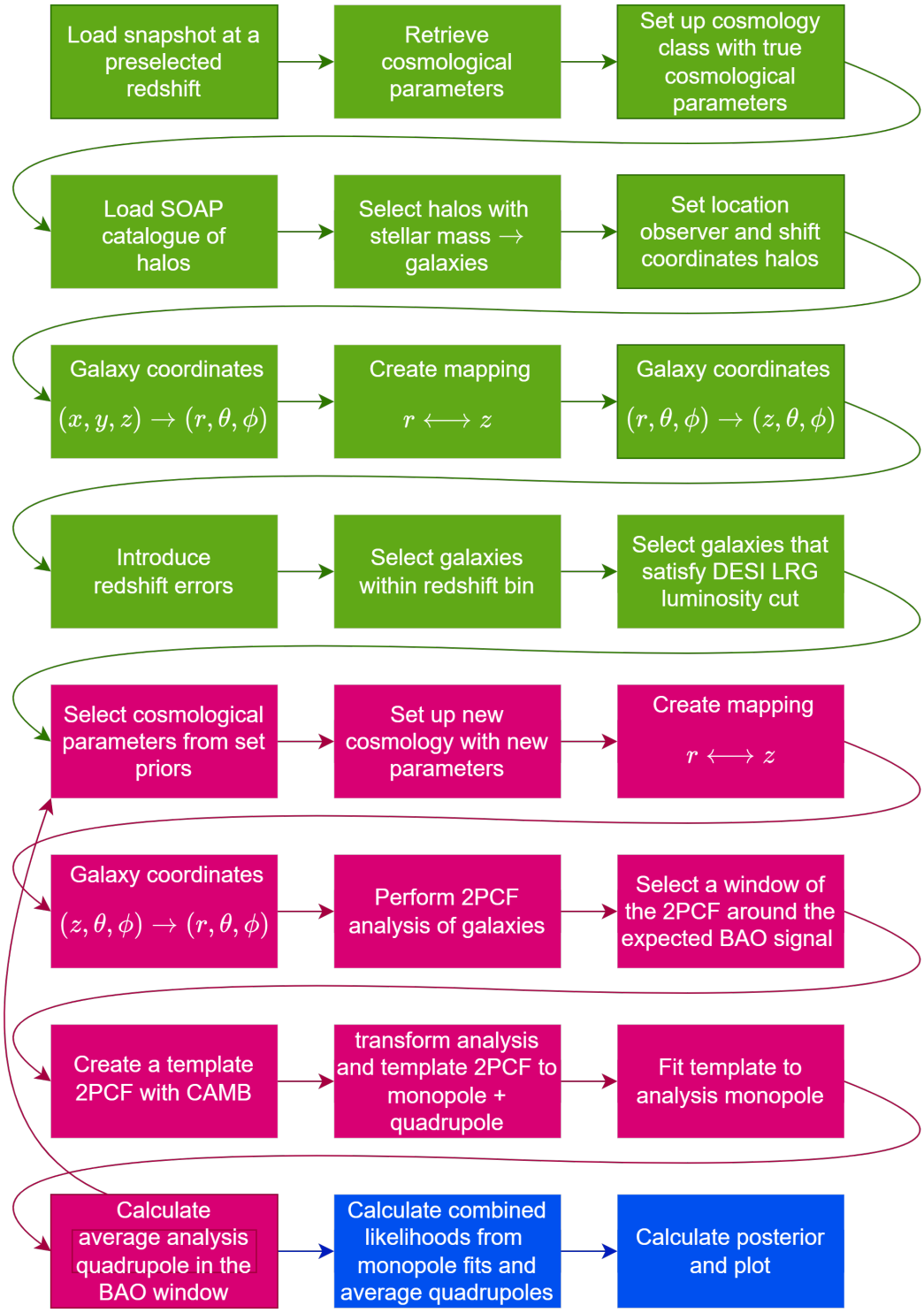

Figure 3.1: *Flow chart of the BAOFLAMINGO pipeline. The analysis pipeline is publicly available at https://github.com/stankortmann/BAO_FLAMINGO*

3.2.2 Mock survey construction and target selection (green blocks)

Snapshot selection

For each redshift bin $[z_{\min}, z_{\max}]$, we load the simulation snapshot at the bin centre $z_c = (z_{\min} + z_{\max})/2$ (e.g. the $z = 0.5$ snapshot for $0.45 < z < 0.55$), which limits redshift-evolution systematics within the bin.

True cosmology initialization

We extract the cosmological parameters from the simulation metadata and initialize a cosmology class using these values. This "true cosmology" is then used for all baseline distance–redshift conversions.

Halo catalogue and stellar-mass filtering

Halos are loaded from the SOAP–HBT catalogue and their centre-of-mass coordinates are used as galaxy position proxies. All coordinates are comoving Cartesian (x, y, z). Halos with zero stellar mass are removed to ensure the remaining sample has non-zero probability of being an observable galaxy and to reduce computational cost.

Observer placement and periodic translations

An observer is placed so that the outer edge of the redshift bin corresponds to the desired comoving radial depth inside the periodic simulation box. We compute the comoving distance corresponding to $z_{\max}$ using the true cosmology and position the observer accordingly. A random translation $(\Delta x, \Delta y, \Delta z)$ is applied to exploit translational invariance under periodic boundary conditions. Different viewing directions (e.g. $x^{\pm}$, $y^{\pm}$, $z^{\pm}$) are implemented via axis rotations.

Spherical coordinate transformation

Coordinates are transformed relative to the observer:

$$(x, y, z) \rightarrow (r, \theta, \phi). \tag{3.10}$$

Version of February 12, 2026– Created February 12, 2026 - 20:24

Distance–redshift mapping

We compute the line-of-sight comoving distance

$$D_C(z) = c \int_0^z \frac{dz'}{H(z')}, \tag{3.11}$$

and the transverse comoving distance

$$D_M(z) = \begin{cases} \dfrac{c}{H_0\sqrt{\Omega_k}} \sinh\left(\sqrt{\Omega_k}\,\dfrac{H_0}{c} D_C(z)\right), & \Omega_k > 0, \\ D_C(z), & \Omega_k = 0, \\ \dfrac{c}{H_0\sqrt{|\Omega_k|}} \sin\left(\sqrt{|\Omega_k|}\,\dfrac{H_0}{c} D_C(z)\right), & \Omega_k < 0. \end{cases} \tag{3.12}$$

We numerically invert this mapping to obtain $z(r)$ where $r \equiv D_M$. In all of the cosmologies we use $\Omega_k \approx 0$. This means that $r \equiv D_c$.

Transform to observed coordinates and apply redshift errors

We map $(r, \theta, \phi) \to (z, \theta, \phi)$ and perturb the redshifts with DESI-like uncertainties:

$$z_{\text{obs}} \sim \mathcal{N}(z_{\text{true}}, \sigma_z^2), \qquad \sigma_z = 0.0005(1+z), \tag{3.13}$$

consistent with DESI LRG target selection. [29] We then keep only objects with $z_{\min} \le z_{\text{obs}} \le z_{\max}$.

DESI LRG colour–magnitude selection

Apparent magnitudes are computed from absolute magnitudes using the luminosity distance,

$$D_L(z) = (1+z)\, D_M(z), \qquad m = M + 5\log_{10}\left(\frac{D_L}{10\ \text{pc}}\right), \tag{3.14}$$

where $D_M(z)$ is the transverse comoving distance obtained from the distance–redshift relation of the (true) cosmology used to construct the mock observation. For each selected subhalo, apparent magnitudes are evaluated in the g, r, and z optical bands and the mid-infrared W1 band. The g, r, z magnitudes are taken directly from the simulation catalogue, while the W1-band magnitude is obtained by extrapolation assuming a linear relation in logarithmic magnitude space. The z, r and g are GAMA bands [30] and W1 is a near infrared band.

Version of February 12, 2026– Created February 12, 2026 - 20:24

We then apply the DESI luminous red galaxy (LRG) target selection, designed to isolate massive, passively evolving galaxies with red colours.[29] The cuts are expressed in terms of apparent magnitudes as:

$$\begin{aligned}
&(z - \mathrm{W1}) > 0.8\,(r - z) - 0.6 \\
&(g - \mathrm{W1} > 2.9) \ \vee \ (r - \mathrm{W1} > 1.8) \\
&(r - \mathrm{W1}) > 1.8\,(\mathrm{W1} - 17.14) \ \text{AND} \\
&(r - \mathrm{W1} > \mathrm{W1} - 16.33) \ \vee \ (r - \mathrm{W1} > 3.3)
\end{aligned}$$

with

$$\begin{aligned}
\lambda_g &= 475\ \text{nm} \\
\lambda_r &= 622\ \text{nm} \\
\lambda_z &= 905\ \text{nm} \\
\lambda_{W1} &= 3368\ \text{nm}.
\end{aligned}$$

These colour–magnitude criteria define a well-separated locus in optical–infrared colour space, suppressing contamination from blue, star-forming galaxies and preferentially selecting luminous systems with high stellar mass.

Luminous red galaxies form an optimal tracer population for BAO measurements because their high large-scale bias enhances the clustering signal, their red spectral energy distributions lead to stable colour selection and precise redshift determination, and their smoothly varying selection function minimizes redshift dependent systematics that could distort the BAO feature when making real life observations. [29]

Version of February 12, 2026– Created February 12, 2026 - 20:24

3.2.3 Visual illustration of the selection pipeline

To illustrate how the ideal underlying matter distribution is progressively transformed into an observationally realistic galaxy sample, we construct a sequence of projected maps from the L1000N1800/HYDRO_FIDUCIAL FLAMINGO simulation (`FID` in Table 4.1 for simulation parameters). A snapshot at $z = 0.5$ is used.
Each panel shows a thin comoving slice of thickness 40 Mpc, corresponding to the range

$$480 \leq z_{\text{box}} \leq 520\,\text{Mpc},$$

projected onto the (x, y) plane. The stellar mass surface density is displayed on a logarithmic scale where indicated. A reference bar corresponding to the BAO scale of 150 Mpc is shown in the lower-right corner of each panel for visual comparison. Halo centres from the SOAP–HBT catalogue are marked with green points.

In principle, cosmological information is encoded in the full matter density field and its power spectrum. However, the total matter distribution cannot be observed directly. Instead, galaxy surveys detect only luminous galaxies that emit sufficient light in observable bands. This introduces bias, incompleteness, and selection effects that alter the effective tracer population. The sequence below demonstrates how successive observational cuts reduce the tracer density and modify the clustering sample used for BAO measurements inside the pipeline.

Version of February 12, 2026– Created February 12, 2026 - 20:24

(1) Stellar mass surface density field Fig. 3.2 shows the logarithmic stellar mass surface density in the selected slice. The cosmic web structure is clearly visible. The BAO reference scale is comparable to the separation between prominent overdense regions, illustrating that the acoustic feature is imprinted on large-scale structure.

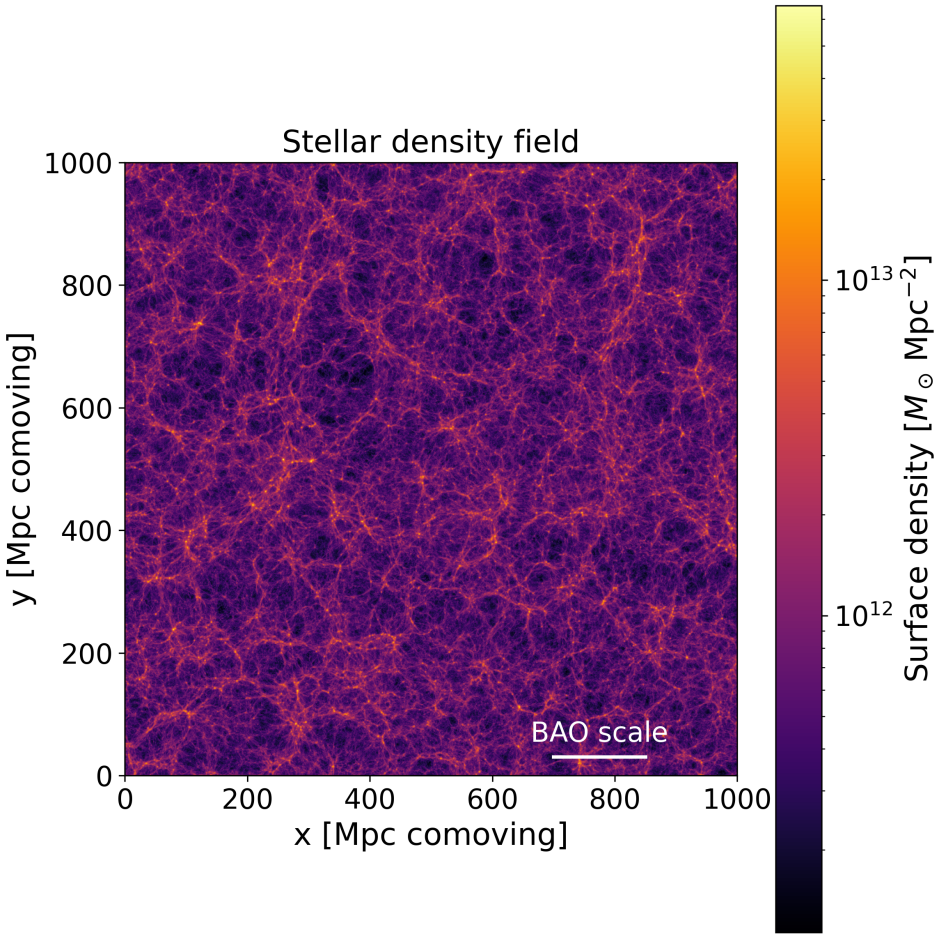

Figure 3.2: *Logarithmic stellar mass surface density in a* 40 Mpc *comoving slice of the* `FID` *simulation. The* 150 Mpc *BAO reference scale is shown in the lower right corner.*

Version of February 12, 2026– Created February 12, 2026 - 20:24

(2) Density field with halos In Fig. 3.3, all halos from the SOAP–HBT catalogue are plotted on the density field, corresponding to

$$N_{\text{tracer}} \approx 7.1 \times 10^5.$$

Halos trace the high density regions of the cosmic web while also populating intermediate density environments. At this stage, the catalogue represents the full halo population of the respective slice of the simulation volume.

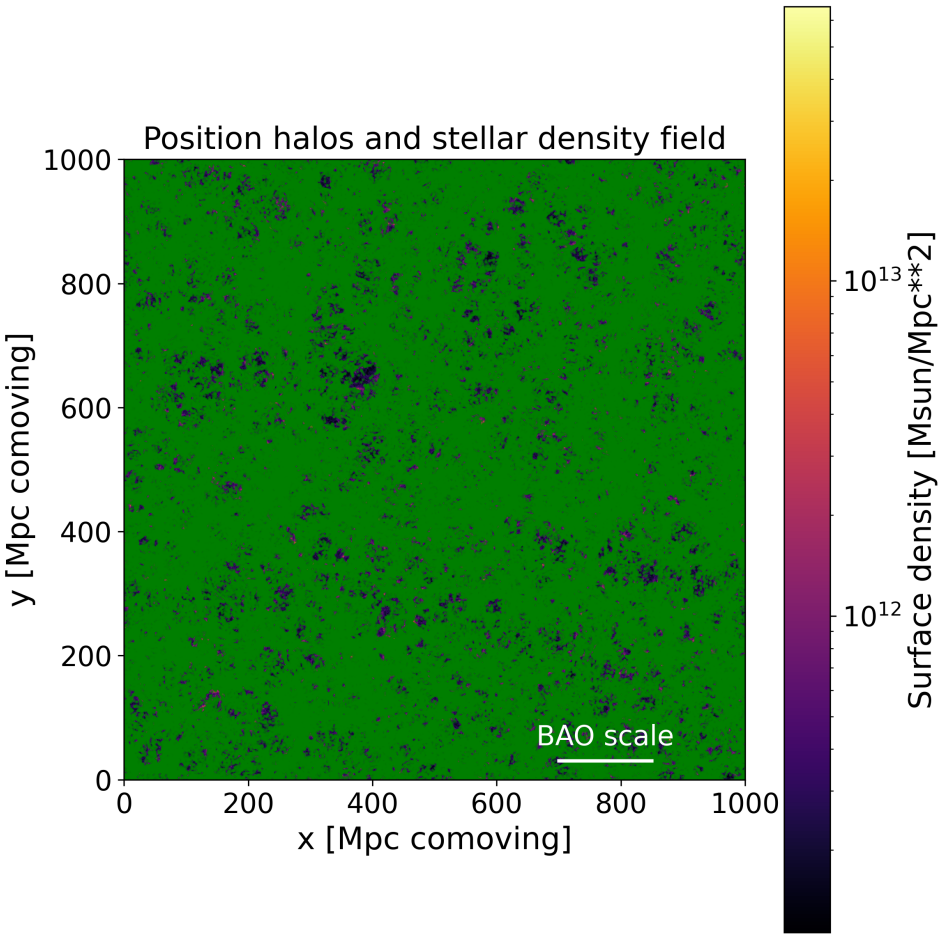

Figure 3.3: *All SOAP–HBT halos ($N_{\text{tracer}} \approx 7.1 \times 10^5$) overlaid on the logarithmic stellar mass surface density field. Green points indicate halo centres.*

Version of February 12, 2026– Created February 12, 2026 - 20:24

(3) Halos only Fig. 3.4 shows only the halo centres without the background density field. The large-scale clustering pattern remains evident despite the discrete sampling, demonstrating that halo tracers alone capture the large-scale modes responsible for the BAO signal.

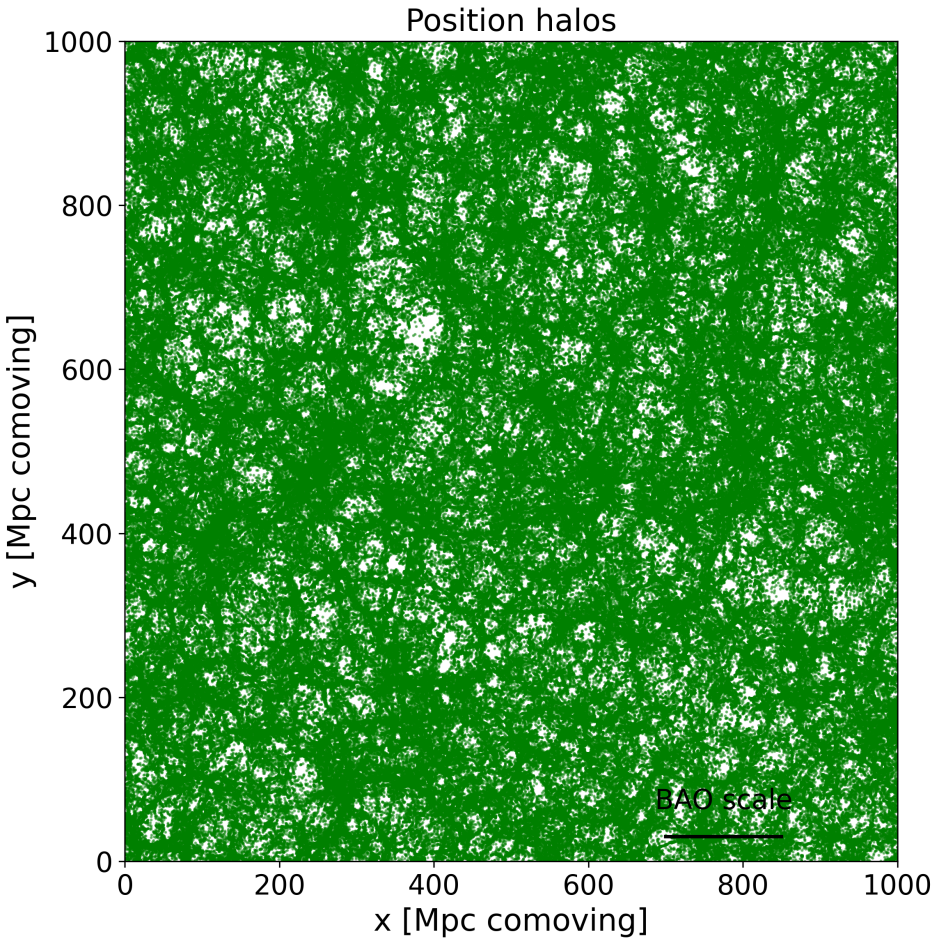

Figure 3.4: *Spatial distribution of all SOAP–HBT halos in the slice ($N_{\mathrm{tracer}} \approx 7.1 \times 10^5$), without the underlying density field.*

Version of February 12, 2026– Created February 12, 2026 - 20:24

(4) Luminous halos detectable in GAMA bands We next restrict the sample to halos hosting galaxies with non-zero stellar mass and detectable emission in the nine GAMA photometric bands. This reduces the sample to

$$N_{\text{tracer}} \approx 4.3 \times 10^4.$$

The resulting distribution (Fig. 3.5) is visibly sparser, with low-mass halos in underdense regions preferentially removed.

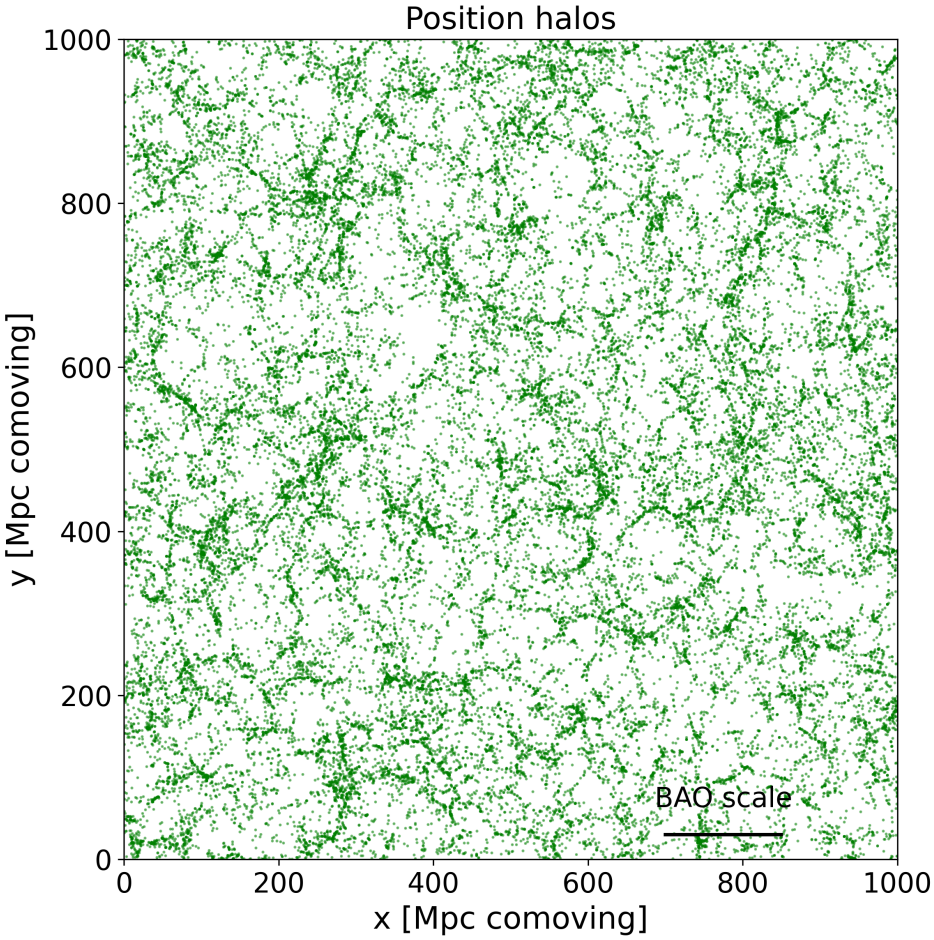

Figure 3.5: *Halos hosting galaxies with detectable emission in the nine GAMA bands ($N_{\text{tracer}} \approx 4.3 \times 10^4$). The tracer population becomes visibly sparser.*

Version of February 12, 2026– Created February 12, 2026 - 20:24

(5) Luminous halos detectable in GAMA bands with stellar mass density Fig. 3.6 overlays the luminous tracer sample on the logarithmic stellar mass density field. The selected galaxies preferentially occupy dense nodes and filaments, reflecting galaxy bias relative to the underlying matter distribution.

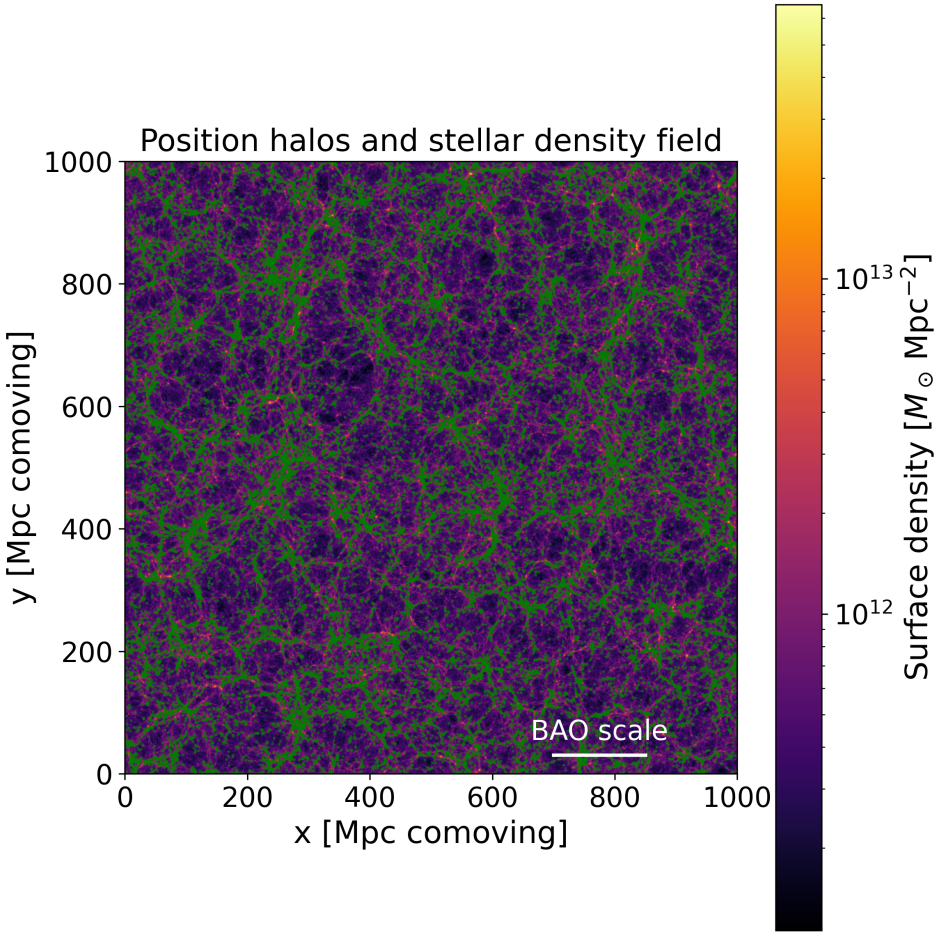

Figure 3.6: *Luminous tracer sample ($N_{\text{tracer}} \approx 4.3 \times 10^4$) with the logarithmic stellar mass surface density field.*

Version of February 12, 2026– Created February 12, 2026 - 20:24

(6) Redshift selection We then apply the radial filter corresponding to the chosen redshift bin ($0.45 \leq z \leq 0.55$) in the mock survey construction. The mock observer is located to the right of the projected slice parallel to the (x, y) plane and at coordinate $z = 500$ Mpc. Only galaxies within the appropriate comoving distance interval are retained, reducing the sample to

$$N_{\text{tracer}} \approx 1.4 \times 10^4.$$

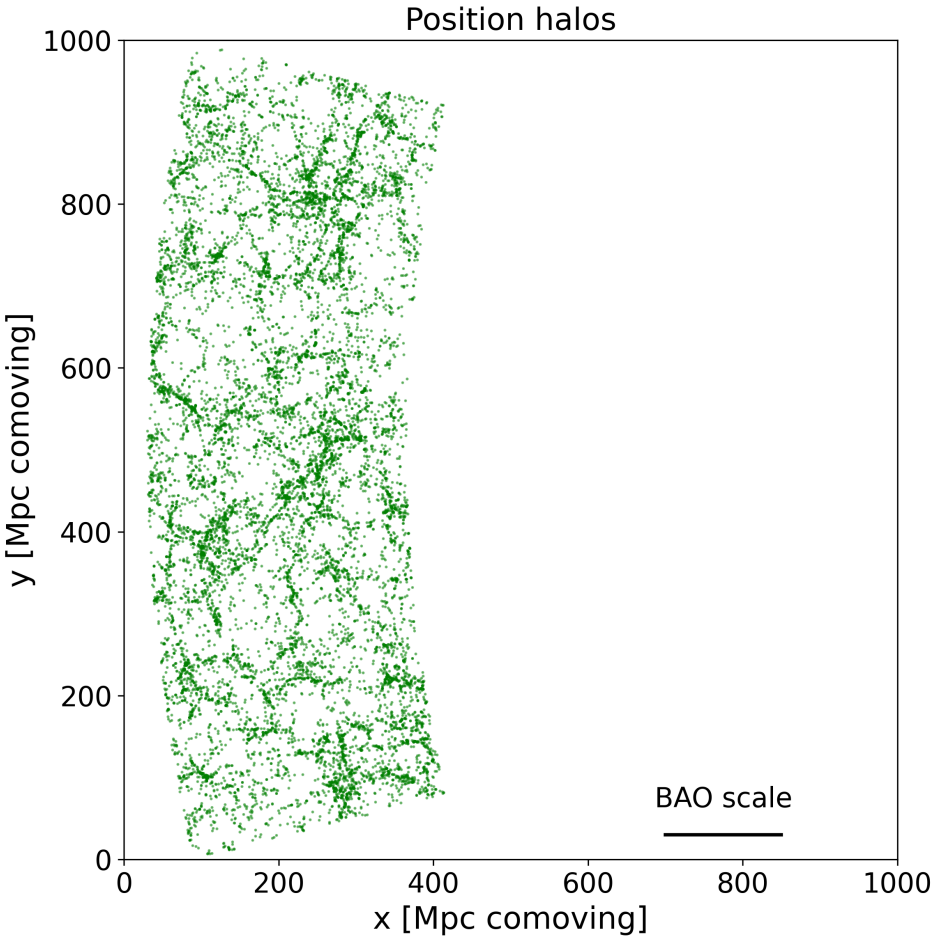

Figure 3.7: *Tracer population after applying the redshift selection relative to the mock observer on the right ($N_{\text{tracer}} \approx 1.4 \times 10^4$).*

(7) DESI LRG colour–magnitude selection Finally, the DESI luminous red galaxy (LRG) colour–magnitude cuts described in Section 3.2.2 are applied. This produces the final mock survey sample with

$$N_{\text{tracer}} \approx 1.4 \times 10^3.$$

The resulting distribution (Fig. 3.8) is significantly sparser and preferentially traces the most massive, highly biased structures. This population constitutes the effective tracer set used for the two-point correlation function BAO analysis.

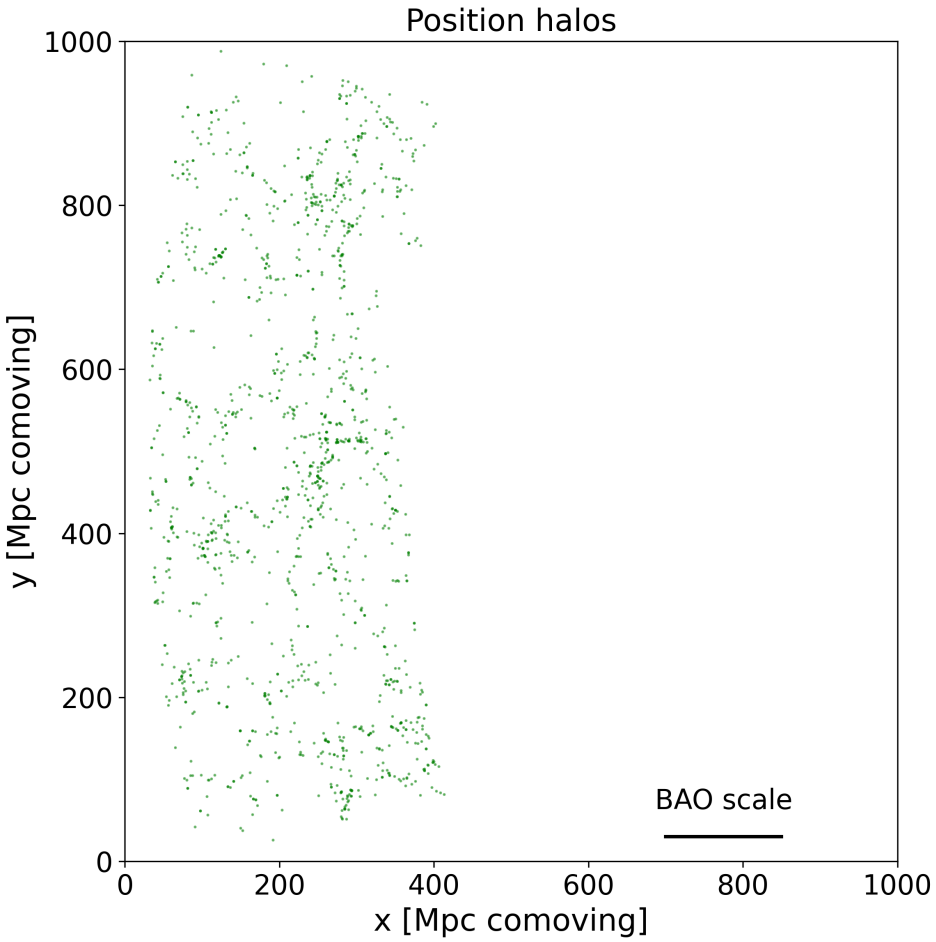

Figure 3.8: *Final DESI LRG-selected tracer population ($N_{\text{tracer}} \approx 1.4 \times 10^3$) used for the BAO analysis.*

At this point, an observer-based realisation of the simulation is defined at fixed redshifts, corresponding to thin radial shells centred around selected epochs. Each shell represents a snapshot of the galaxy distribution as it would be observed in a redshift survey such as SDSS or DESI. When considered individually, these shells are analysed separately in this work; however, taken together across multiple redshifts they would form a continuous lightcone geometry, with galaxies occupying a spherical wedge extending outward from the observer, as illustrated in Fig. 3.9.

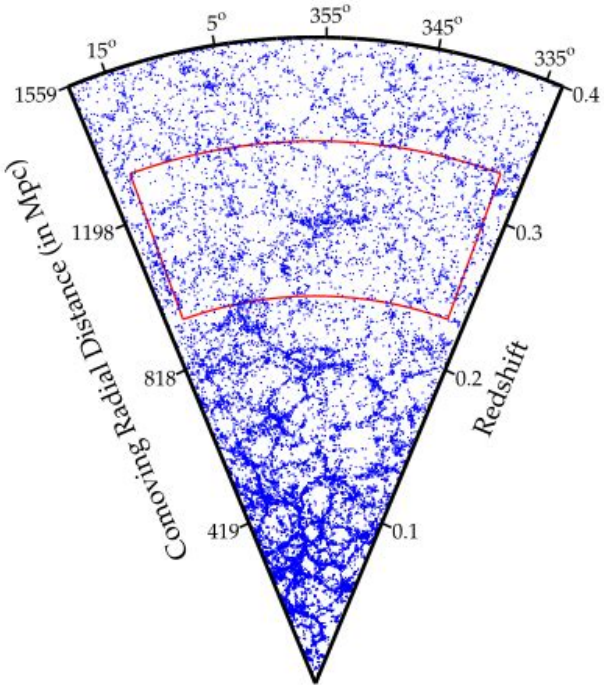

Figure 3.9: *Illustration of the SDSS galaxy survey in lightcone coordinates, shown as a compressed two dimensional projection in (z, ϕ) space. The radial direction corresponds to redshift, which is mapped to comoving radial distance D_c assuming a fiducial cosmological model, while the angular extent defines the survey footprint. This figure is adapted from the SDSS data release paper.[31]*

3.2.4 Averaging over correlated observer realizations

To improve statistical precision, multiple observer realizations are generated by randomly translating the galaxy catalogue within the periodic simulation volume. Since all realizations probe the same underlying density field, they are not statistically independent and share large scale modes. Each realization i is assigned a weight

$$w_i = \frac{f_i n_i}{\sum_j f_j n_j}, \tag{3.15}$$

where f_i is the fractional survey volume and n_i the galaxy number density. The averaged correlation function is

$$\bar{\boldsymbol{\xi}} = \sum_i w_i \boldsymbol{\xi}^{(i)}. \tag{3.16}$$

Assuming a constant average overlap ρ between realizations, the covariance of the averaged measurement is

$$\mathrm{Cov}(\bar{\boldsymbol{\xi}}) = \sum_i \left[w_i^2 + \rho\, w_i (1 - w_i) \right] \mathbf{C}^{(i)}. \tag{3.17}$$

Version of February 12, 2026– Created February 12, 2026 - 20:24

3.2.5 Cosmology variation and 2PCF measurement (pink blocks, MPI)

Trial cosmologies and remapping

For each parameter combination in a predefined grid of priors, we initialize a new cosmology object and recompute the mapping $r \leftrightarrow z$. The observed coordinates are then converted back to comoving space as

$$(z, \theta, \phi) \rightarrow (r, \theta, \phi), \tag{3.18}$$

creating a 3D map as interpreted under the trial cosmology.

Two-point correlation function with `pycorr`

We measure the anisotropic two-point correlation function (2PCF) $\xi(s, \mu)$ using the publicly available `pycorr` package [32, 33]. The estimator adopted throughout this work is the Landy–Szalay estimator [34],

$$\xi(s, \mu) = \frac{DD(s, \mu) - 2DR(s, \mu) + RR(s, \mu)}{RR(s, \mu)}, \tag{3.19}$$

where DD, DR, and RR denote the suitably normalized counts of data–data, data–random, and random–random pairs in bins of separation s and cosine of the line-of-sight angle μ. This estimator is known to be nearly minimum-variance and to efficiently suppress edge effects arising from complex survey geometries.

The separation s is defined as the comoving distance between galaxy pairs, while μ is the cosine of the angle between the pair separation vector and the line of sight, defined using the midpoint of the pair. This choice ensures a symmetric treatment of the two galaxies in each pair and is standard in anisotropic clustering analyses. [35]

Random catalogues are constructed to have the same angular and radial selection functions as the data. Angular positions are drawn uniformly over the spherical wedge footprint using

$$\phi \sim \mathcal{U}[\phi_{\min}, \phi_{\max}] \qquad \cos\theta \sim \mathcal{U}[\cos\theta_{\min}, \cos\theta_{\max}]$$

which ensures uniform sampling on the sphere. The radial selection function is modeled by estimating the empirical redshift distribution $n(z)$ of the selected galaxies, constructing a histogram of this distribution, and interpolating it to obtain a smooth probability density. Random redshifts are drawn from this distribution and converted to comoving distances using the same trial cosmology employed for the data, thereby guaranteeing consistency between the data and random catalogues.

The random catalogues contain a factor of 20 more objects than the data in order to reduce Poisson noise in the RR and DR pair counts. Tests confirm that increasing the random density beyond this factor does not significantly change the measured correlation function within the statistical uncertainties.

Covariances of $\xi(s, \mu)$ are estimated using jackknife resampling. [36] The survey wedge is divided into equal-area angular regions using a HEALPix tessellation. [37] The 2PCF is recomputed by omitting one region at a time, and the covariance matrix is estimated as

$$C_{ij} = \frac{N_{\mathrm{JK}} - 1}{N_{\mathrm{JK}}} \sum_{k=1}^{N_{\mathrm{JK}}} \left[\xi_i^{(k)} - \bar{\xi}_i\right] \left[\xi_j^{(k)} - \bar{\xi}_j\right], \tag{3.20}$$

where N_{JK} is the number of jackknife regions, $\xi_i^{(k)}$ is the measurement in bin i for the k-th jackknife sample, and $\bar{\xi}_i$ is the mean over all jackknife realizations. Jackknife resampling provides a robust, internally consistent estimate of the covariance on BAO scales and is widely used in large-scale structure analyses. [29, 36]

Version of February 12, 2026– Created February 12, 2026 - 20:24

BAO fitting window

We restrict the analysis to separations near the BAO scale, typically $s \in [s_{\mathrm{BAO}} - 50, s_{\mathrm{BAO}} + 50]$ Mpc, with $s_{\mathrm{BAO}} \approx 150$ Mpc.

Theoretical template from CAMB

We compute a theoretical correlation-function template using CAMB. [15] The linear matter power spectrum is evaluated over

$$k \in [10^{-4}, 10]\ \mathrm{Mpc}^{-1}, \tag{3.21}$$

which safely brackets all scales contributing to the BAO feature. The lower bound captures large-scale modes relevant for the broadband correlation function, while the upper bound includes all small-scale power affecting the BAO peak shape. Contributions from higher wavenumbers are negligible at separations $s \sim 150$ Mpc.
The correlation function is obtained via

$$\xi(r) = \frac{1}{2\pi^2} \int_0^\infty dk\, k^2 P(k) \frac{\sin(kr)}{kr}. \tag{3.22}$$

For $w_0 w_a$CDM cosmologies we use the PPF prescription to allow stable evolution across the phantom divide. [38] The template is computed on a wider separation range than the data 2PCF to avoid extrapolation of the template when applying a dilation parameter α.

Version of February 12, 2026– Created February 12, 2026 - 20:24

Multipole projection and covariance transformation

We compute the monopole and quadrupole via Legendre projection:

$$\xi_\ell(s) = \frac{2\ell+1}{2} \int_{-1}^{1} d\mu\, \xi(s,\mu)\, P_\ell(\mu), \qquad \ell \in \{0,2\}. \tag{3.23}$$

If $\mathbf{x}$ is the flattened 2D data vector and $\mathbf{y}$ the stacked multipole vector, then $\mathbf{y} = \mathbf{P}\mathbf{x}$ and the covariance transforms as

$$\mathbf{C}_{\text{multi}} = \mathbf{P}\, \mathbf{C}_{2D}\, \mathbf{P}^{\mathsf{T}}. \tag{3.24}$$

An example for the CAMB template monopole at $z = 0.5$ is seen in Fig. 3.10

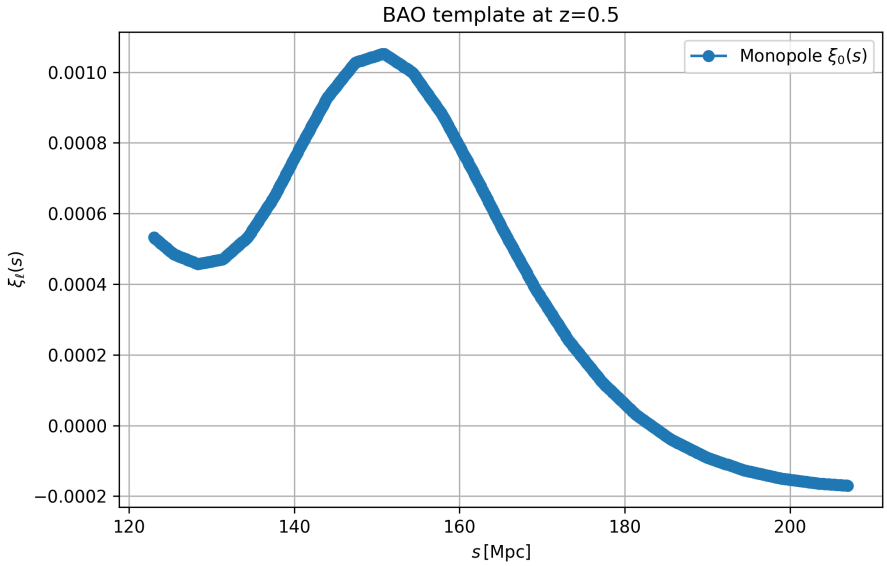

Figure 3.10: *Monopole of the BAO template at $z = 0.5$ created by the CAMB Python package.*

Monopole BAO fit with dilation and nuisance terms

We fit the monopole using a dilated template plus a broadband polynomial:

$$\xi_0^{\rm model}(s) = b^2\,\xi_0^{\rm temp}\left(\frac{s}{\alpha}\right) + \sum_{i=0}^{2} a_i s^i, \tag{3.25}$$

where b is an effective bias amplitude, α is the BAO dilation parameter (with $\alpha = 1$ corresponding to no shift), and the polynomial absorbs smooth broadband mismatches. [39, 40] The parameters $(\alpha, b, \{a_i\})$ are determined by minimizing a χ^2 statistic that quantifies the mismatch between the measured monopole $\xi_0^{\rm data}(s)$ and the model prediction $\xi_0^{\rm model}(s)$. Explicitly, the χ^2 statistics is defined below:

$$\chi^2(\alpha, b, a_i) = \sum_{i,j} \left[\xi_0^{\rm data}(s_i) - \xi_0^{\rm model}(s_i|\alpha, b, a_i)\right] C_{ij}^{-1} \left[\xi_0^{\rm data}(s_j) - \xi_0^{\rm model}(s_j|\alpha, b, a_i)\right] \tag{3.26}$$

where C_{ij} is the covariance matrix of the monopole measurement and the sums run over separation bins within the BAO fitting range.
The best-fitting BAO dilation parameter α is obtained by minimizing χ^2 with respect to all free parameters. In this framework, deviations of α from unity quantify shifts of the BAO scale relative to the fiducial template, while the nuisance terms absorb smooth broadband differences without altering the position of the acoustic feature as we have qualitatively checked. We extract α and σ_α from each fit.

Quadrupole isotropy diagnostic

We compute the quadrupole $\xi_2(s)$ and average it over the BAO window($< \xi_2(100 \le s \le 200, \mu) >$). In the isotropic limit $\xi(s, \mu) = \xi(s)$,

$$\xi_2(s) = \frac{5}{2}\int_{-1}^{1} d\mu\; \xi(s,\mu)\, P_2(\mu) = \frac{5}{2}\xi(s)\int_{-1}^{1} d\mu\; P_2(\mu) = 0, \tag{3.27}$$

since $\int_{-1}^{1} P_2(\mu) d\mu = 0$.Non-zero quadrupole reflects line-of-sight anisotropy from redshift-space distortions and/or incorrect distance conversions. [35, 41] This means the following discrete function will be applied to all cosmologies and the value of $\langle \xi_2 \rangle_{100 \le s \le 200}$ extracted:

$$\langle \xi_2 \rangle_{100 \le s \le 200} = \frac{1}{N_s} \sum_{s_i \in [100,200]} \xi_2(s_i) \tag{3.28}$$

3.2.6 Likelihoods and posterior inference (blue blocks)

Gaussian likelihoods

For each cosmology-grid point we obtain (α, σ_α) and optionally $(\bar{\xi}_2, \sigma_{\bar{\xi}_2})$. We define Gaussian likelihoods:

$$\mathcal{L}_\alpha(\theta) \propto \exp\left[-\frac{1}{2}\left(\frac{\alpha(\theta)-1}{\sigma_\alpha(\theta)}\right)^2\right], \tag{3.29}$$

and optionally

$$\mathcal{L}_{\rm quad}(\theta) \propto \exp\left[-\frac{1}{2}\left(\frac{\bar{\xi}_2(\theta)}{\sigma_{\bar{\xi}_2}(\theta)}\right)^2\right]. \tag{3.30}$$

Combining redshift bins

Assuming independent redshift bins, the combined likelihood is

$$\mathcal{L}_{\rm comb}(\theta) = \prod_i \mathcal{L}_i(\theta), \qquad \ln \mathcal{L}_{\rm comb} = \sum_i \ln \mathcal{L}_i. \tag{3.31}$$

In practice, bins are not perfectly independent in a single simulation volume due to shared large-scale modes; multiple independent simulation realizations would be required for strict independence.

3.2.7 Validation and systematics

A series of validation tests and systematic checks were performed to ensure that the recovered BAO signal and inferred cosmological constraints are robust.

Recovery of the true cosmology As a primary consistency check, the analysis was performed using the true cosmological parameters of the simulation. In this case, the recovered BAO dilation parameter is expected to satisfy $\alpha \approx 1$. We find that α deviates from unity by at most $\sim 5\%$, with the deviation increasing mildly with redshift. This behaviour is consistent with the decreasing number density of galaxies at higher redshift, which increases statistical noise in the correlation function measurement. The recovery of $\alpha \simeq 1$ demonstrates that the pipeline does not introduce a systematic shift in the BAO scale.

Version of February 12, 2026– Created February 12, 2026 - 20:24

Observer placement, averaging, and error estimation To test sensitivity to observer placement and finite-volume effects, the analysis was repeated for multiple random translations of the galaxy catalogue within the periodic simulation volume. Due to the finite box size, these observer realizations are not fully independent. The number of statistically independent realizations is limited by the ratio

$$N_{\mathrm{ind}} \sim \frac{V_{\mathrm{simulation}}}{V_{\mathrm{survey}}}, \tag{3.32}$$

which depends on the redshift bin, as higher redshift bins probe a smaller comoving volume. For the $L = 1000\,\mathrm{Mpc}$ FLAMINGO simulation, this typically results in only a few effectively independent observer placements at low redshift, increasing at higher redshift.

Rather than treating each observer realization as independent, the two-point correlation function is averaged across realizations and uncertainties are propagated accordingly. For each observer placement i, the anisotropic correlation function $\xi_i(s,\mu)$ and its covariance $\mathbf{C}_i$ are measured. The averaged correlation function is computed as

$$\bar{\xi}(s,\mu) = \sum_{i=1}^{N} w_i\, \xi_i(s,\mu), \tag{3.33}$$

with weights

$$w_i = \frac{V_i n_i}{\sum_j V_j n_j}, \tag{3.34}$$

where V_i is the fractional survey volume and n_i the galaxy number density of realization i. This weighting reflects the relative statistical power of each realization and mitigates the effect of partially overlapping volumes.

Because the observer realizations are drawn from the same periodic simulation, their measurements are correlated through shared large-scale modes. Following standard treatments of correlated mock catalogues, the averaged covariance is constructed as

$$\bar{\mathbf{C}} = \sum_{i=1}^{N} \beta_i\, \mathbf{C}_i, \tag{3.35}$$

with

$$\beta_i = w_i^2 + \rho\, w_i(1 - w_i), \tag{3.36}$$

where $\rho = \frac{1}{N_{indenpent}}$ is the mean fractional survey volume relative to the simulation box. The first term corresponds to standard weighted errors, while the second term accounts for correlations induced by overlapping density modes due to observing the same region of the simulation. This prescription interpolates between the limits of independent and fully correlated measurements, as discussed in [42] and [43].
This approach ensures that uncertainties are not underestimated by treating correlated observer realizations as independent while still exploiting the statistical gain available from multiple observer placements within the periodic simulation volume.

Random catalogue construction The impact of the random catalogue was tested by varying the random seed and verifying that the measured correlation function and BAO fit parameters remained stable. A random catalogue size of $N_R = 20N_D$ was found sufficient to suppress Poisson noise in the RR and DR pair counts. The radial selection function $n(z)$, estimated from a histogram and smoothed with a mild Gaussian kernel, was confirmed to reproduce the observed redshift distribution of the data. The result of the test at $0.45 \leq z \leq 0.55$ inside a ΛCDM simulation can be seen in Fig. 3.11.

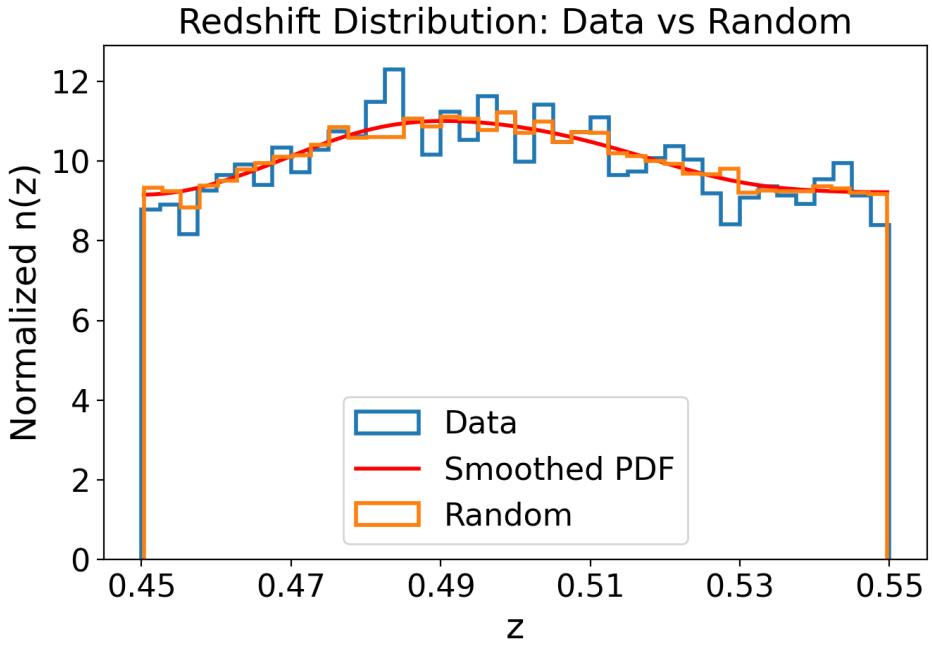

Figure 3.11: *Normalized $n(z)$ with $0.45 \leq z \leq 0.55$. The redshifts of the random catalogue are drawn from the smoothed PDF.*

Binning choices The dependence of the results on binning was explored by varying the number of separation and angular bins. A clear trade-off between resolution and noise was observed: finer binning increases noise without improving BAO scale recovery, while coarser binning smooths the BAO feature. The adopted binning scheme was found to provide a stable compromise between these effects.

Covariance estimation The jackknife covariance was validated by monitoring the stability of the monopole autocovariance across multiple realizations. Using 100 HEALPix-based angular jackknife regions yielded a covariance matrix whose diagonal elements varied only weakly between realizations, indicating that the covariance estimate is sufficiently stable for the purposes of this analysis.

Version of February 12, 2026– Created February 12, 2026 - 20:24

Broadband modeling and BAO fitting The robustness of the BAO fitting procedure was tested by varying the order of the nuisance polynomial used to model broadband shape variations. These broadband effects include nonlinear effects of galaxy formation in the FLAMINGO simulation. Zero- and first-order polynomials were generally insufficient, occasionally biasing the recovered BAO dilation parameter or preventing a stable fit. A second-order polynomial provided the most stable recovery of the BAO scale without visibly overfitting the BAO feature or shifting it.

As an additional consistency check, the relationship between the BAO dilation parameter α and the nuisance polynomial coefficients was examined. Because the broadband terms are not strictly orthogonal to the BAO signal, some degree of covariance between α and the nuisance parameters is expected. However, excessively strong correlations would indicate that the broadband model is partially absorbing shifts in the BAO peak position.

This covariance was therefore monitored qualitatively by inspecting if the peaks in monopole fits were visible by the naked eye. If they were not visible but a fit was still made, these fits could have been induced by the nuisance parameters. A far more rigorous analysis of the covariance between α and the nuissance parameters is needed.

Assumptions and limitations The theoretical template is based on linear theory only and does not explicitly include non-linear BAO damping or reconstruction. These effects primarily modify the broadband shape and peak amplitude rather than the peak position. Since the analysis focuses on relative shifts of the BAO scale and marginalizes over broadband contributions, this approximation is sufficient for the current study. Residual systematics from nonlinear effects are expected to be subdominant compared to statistical uncertainties such as the Poisson noise.[41]

Chapter 4

Results

4.1 Simulations

We analyse a set of cosmological hydrodynamical simulations from the FLAMINGO simulation suite, focusing on the `L1000N1800` configuration. All simulations are evolved from $z = 30$ to $z = 0$ in a periodic cubic volume of comoving side length 1000 Mpc. The simulation contains 1800^3 cold dark matter particles and an equal number of baryonic (gas) particles. The corresponding particle masses are $m_{\mathrm{CDM}} = 5.65 \times 10^9\, M_\odot$ and $m_{\mathrm{b}} = 1.07 \times 10^9\, M_\odot$, respectively.[11]

In this work, we consider three simulation variants: a fiducial ΛCDM cosmology (`FID`), a dark-energy model with evolving equation-of-state parameters consistent with DESI forecasts (`W0WA`), and a corresponding model with enhanced AGN feedback (`W0WA+AGN`).[11] The key cosmological parameters, AGN feedback, and resulting galaxy statistics used in the analysis are summarised in table 4.1.

Table 4.1: *Simulation and survey properties for the fiducial and DESI cosmologies in the FLAMINGO* `L1000N1800` *simulation suite.* `FID` *=* `HYDRO_FIDUCIAL`*,* `WOWA` *=* `HYDRO_DESI_WOWA` *and* `WOWA+AGN` *=* `HYDRO_DESI_WOWA_STRONGEST_AGN`

Simulation	`FID`	`WOWA`	`WOWA+AGN`
H_0 $[\mathrm{km\,s^{-1}\,Mpc^{-1}}]$	68.1	66.8	66.8
$\Omega_{\mathrm{CDM},0}$	0.256	0.268	0.268
$\Omega_{DE,0}$	0.694	0.681	0.681
$\Omega_{\mathrm{b},0}$	0.049	0.050	0.050
w_0	-1	-0.760	-0.760
w_a	0	-0.857	-0.857
AGN feedback	normal	normal	high
Survey redshift bin width Δz	0.1	0.1	0.1
$N_{\mathrm{gal}}(z_{\mathrm{eff}} = 0.5)$	$\approx 28 \times 10^3$	$\approx 30 \times 10^3$	$\approx 40 \times 10^3$
$N_{\mathrm{gal}}(z_{\mathrm{eff}} = 0.7)$	$\approx 13 \times 10^3$	$\approx 13 \times 10^3$	$\approx 16 \times 10^3$
$n_{\mathrm{gal}}(z_{\mathrm{eff}} = 0.5)$ $[\mathrm{deg^{-2}}]$	≈ 37	≈ 38	≈ 51
$n_{\mathrm{gal}}(z_{\mathrm{eff}} = 0.7)$ $[\mathrm{deg^{-2}}]$	≈ 28	≈ 28	≈ 35

Version of February 12, 2026– Created February 12, 2026 - 20:24

4.2 Validation by constraining Ω_m and Ω_{DE}

The first step in validating the BAO analysis pipeline is to test whether the simulation is able to recover the matter density parameter Ω_m while keeping all other cosmological parameters fixed to their fiducial values. $\Omega_m \propto (z+1)^3$ follows from Eq. 2.4. This means Ω_m, apart from radiation ($\Omega_r \propto (z+1)^4$) at very early times , is a dominant component in the early universe. So it has a strong effect on how large the BAO rulers length r_s is in the CAMB template production. This is in addition to the fact that it has a noticeable effect on D_M in the latter stages of the universe and thus influences the shift in the 2PCF data analysis. It can overall be expected that only a very narrow range of Ω_m values give a correct fit due to the effect on both processes.

4.2.1 `FID`

The following (Ω_m, Ω_{DE}) priors were used inside the `FID` simulation:

$$\Omega_m \sim U[0.2, 0.4], \qquad \Omega_{DE} \sim U[0.6, 0.8]$$

The resulting (Ω_m, Ω_{DE}) posterior has a likelihood evaluated on a uniform grid of 10×10 points spanning the chosen prior ranges (including both endpoints) This corresponds to step sizes:

$$\Delta\Omega_m = \frac{0.6-0.4}{10-1} = \frac{0.2}{9} \simeq 0.022 \quad \Delta\Omega_{DE} = \frac{0.8-0.6}{10-1} = \frac{0.2}{9} \simeq 0.022$$

Fig. 4.1 shows that the pipeline is able to recover the a posterior contour in which true values of $\Omega_m = 0.305$ and $\Omega_{DE} = 0.694$ of the `FID` simulation fall within the 68% confidence contour.The pipeline seems to favor cosmologies with a slightly higher Ω_m and Ω_{DE} value but these are nearly within 1σ for both parameter marginals. The posterior is not sampled well enough due to the uniform grid having large $\Delta\Omega_{DE}$ and $\Delta\Omega_m$. Thus the result in 4.1 is more of a validation that the pipeline works than necessarily constraining Ω_m and Ω_{DE} tightly.

$$\begin{aligned} \Omega_m &= 0.31^{+0.02}_{-0.00} \quad (68\%\ \text{CI}) \\ \Omega_{DE} &= 0.73^{+0.03}_{-0.04} \quad (68\%\ \text{CI}) \end{aligned} \tag{4.1}$$

Version of February 12, 2026– Created February 12, 2026 - 20:24

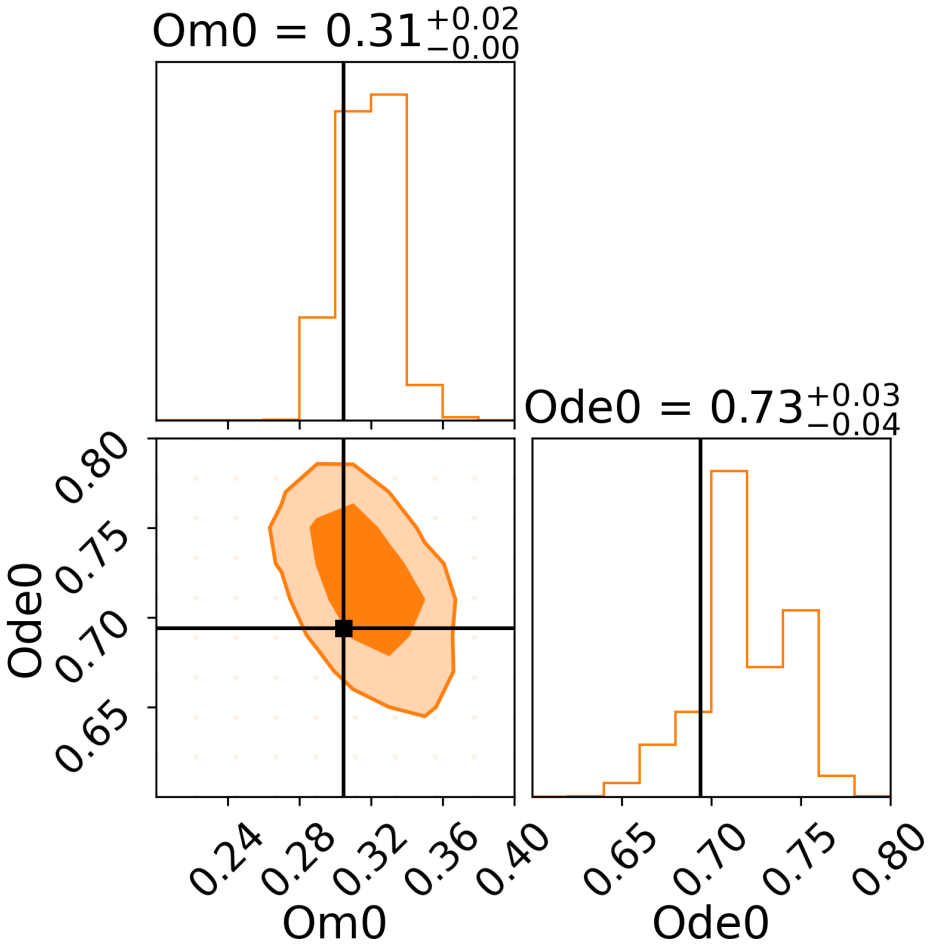

Figure 4.1: *Joint posterior constraints on (Ω_m, Ω_{DE}) from the `FID` simulation using narrow priors, obtained by combining the $z = 0.5$ and $z = 0.7$ redshift shells ($\Delta z = 0.1$). Contours show the 68% and 95% confidence regions. The black lines indicate the true cosmology. The true values of Ω_m and Ω_{DE} are both within 1σ but true cosmology is on the edge of the 68% confidence contour. $N_{realizations} = 6$.*

Version of February 12, 2026– Created February 12, 2026 - 20:24

4.3 w_0 and w_a

In this section the w_0 and w_a are constrained for the 3 simulations. All other cosmological parameters are fixed at their true value of the respective simulation.

4.3.1 Validation of `FID` simulation at $z = 0.5$

The pipeline is first validated by using a small probe within the `FID` simulation using the following priors

$$w_0 \sim U[-1.5, -0.5] \qquad w_a \sim U[-1, 1]$$

The resulting (w_0, w_a) posterior has a likelihood evaluated on a uniform grid of 10×10 points spanning the chosen prior ranges (including both endpoints) This corresponds to step sizes:

$$\Delta w_0 = \frac{-0.5 - (-1.5)}{10 - 1} = \frac{1}{9} \simeq 0.111$$
$$\Delta w_a = \frac{1 - (-1)}{10 - 1} = \frac{2}{9} \simeq 0.222$$

As a consistency check of the BAO analysis pipeline, we examine whether the correct cosmological parameter combination (w_0, w_a) used to generate the `FID` simulation at $z = 0.5$ yields a stable and unbiased BAO recovery. Fig. 4.2 shows the monopole two-point correlation function measured from the simulation together with the best fitting shifted BAO template. The template is obtained by minimizing the χ^2 statistic defined in Eq. 3.26, allowing the BAO dilation parameter α and broadband nuisance terms to vary. The recovered value $\alpha = 0.984$ is close to unity, indicating that the BAO peak position is accurately reproduced when the correct cosmology is assumed.

To further assess the robustness of the result, Fig. 4.3 presents complementary diagnostics based on the BAO dilation parameter and the quadrupole moment. The left panel shows the recovered α values across the (w_0, w_a) grid, where the true simulation cosmology (marked by a cross) lies close to $\alpha = 1$.

The right panel displays the averaged quadrupole $\langle \xi_2 \rangle$ over separations 100–200 Mpc, computed as in Eq. 3.28. The quadrupole remains consistent with zero within uncertainties, and the true cosmology is among the parameter combinations with the smallest anisotropic signal.

Version of February 12, 2026– Created February 12, 2026 - 20:24

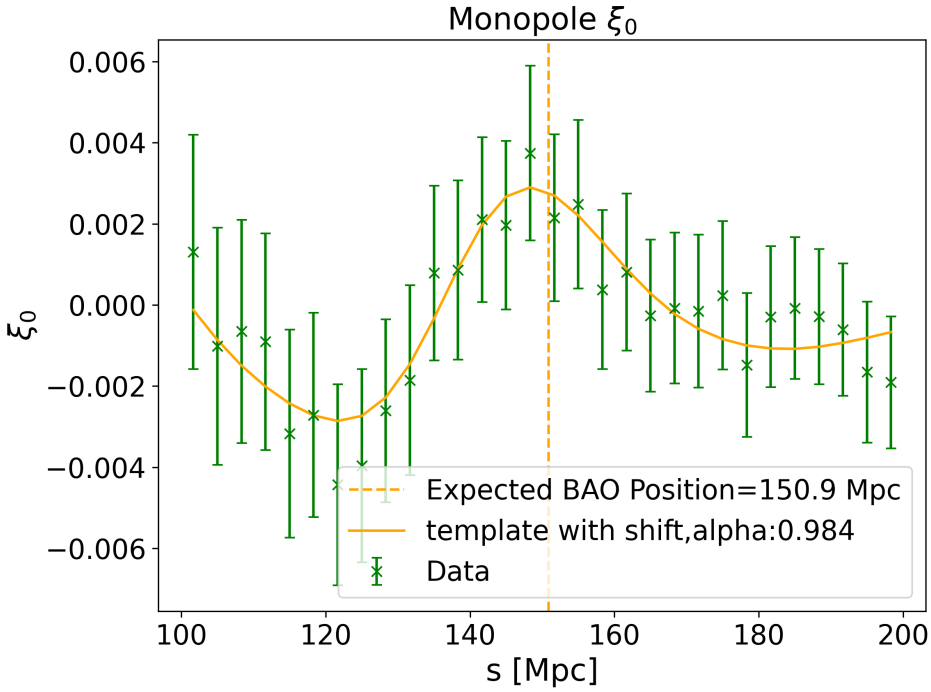

Figure 4.2: *Monopole BAO fit for the* `FID` *simulation (narrow priors) with the correct cosmological values for* (w_0, w_a) *at* $z = 0.5$*. The vertical dotted line indicates the expected BAO peak position in comoving separation (Mpc) for the fiducial template. The green data points with error bars show the measured monopole correlation function* $\xi_0^{\text{data}}(s)$*, while the yellow curve shows the best-fitting shifted template model* $\xi_0^{\text{model}}(s)$ *obtained by minimizing the* χ^2 *defined in Eq. 3.26. The best-fitting dilation parameter is* $\alpha = 0.984$ *(no* σ_α *shown, error is computed internally).* $N_{realisations} = 6$*.*

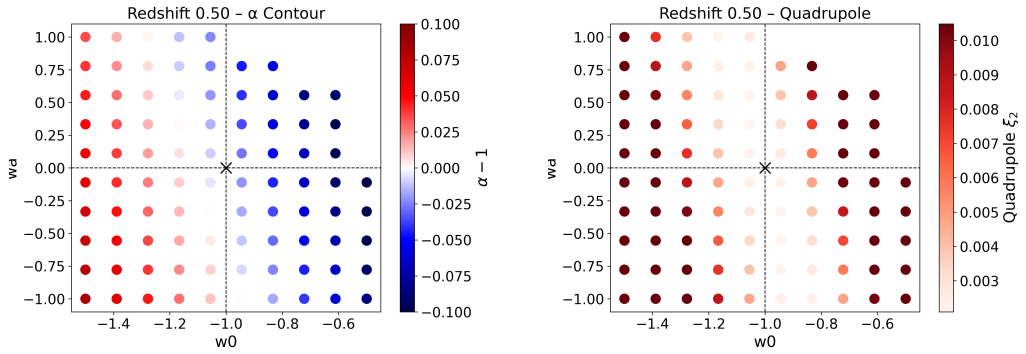

(a) *(b)*

Figure 4.3: *Left: BAO dilation parameter shift α for the* `FID` *simulation with narrow priors at redshift $z = 0.5$, evaluated using Eq. 3.26. Red regions indicate BAO scales larger than the fiducial template, while blue regions correspond to smaller inferred BAO scales. The cross marks the true simulation cosmology and lies close to $\alpha = 1$, indicating good overall recovery. Right: Average quadrupole $\langle \xi_2 \rangle$ measured over separations* 100–200 Mpc *as in Eq. 3.28 for the same configuration. The quadrupole remains consistent with zero within uncertainties, with the true cosmology (cross) being among the cosmologies with the lowest anisotropy. For both quadrupole and α plots we see some points (especially in the top right corner) are blank. This means the pipeline was not able to recover a correct fit for that cosmology. $N_{realisations} = 6$.*

Version of February 12, 2026– Created February 12, 2026 - 20:24

Fig. 4.4 shows that the pipeline is able to recover the a posterior contour in which true values of $w_0 = -1$ and $w_a = 0$ of the `FID` simulation fall within the 68% confidence contour. The posterior is not sampled well enough due to the uniform grid having large Δw_0 and Δw_a. Thus the result in 4.2 is more of a validation that the pipeline works than necessarily constraining w_0 and w_a tightly. It does show that w_a seems to be less tightly constrained than w_0. Another observation is that the (w_0, w_a) posterior is not fully encapsulated by the prior choice made before. It is therefore needed to choose wider priors on both parameters to fully show the posterior.

$$\begin{aligned} w_0 &= -1.06^{+0.11}_{-0.11} \quad (68\%\ \text{CI}) \\ w_a &= -0.26^{+0.59}_{-0.74} \quad (68\%\ \text{CI}) \end{aligned} \tag{4.2}$$

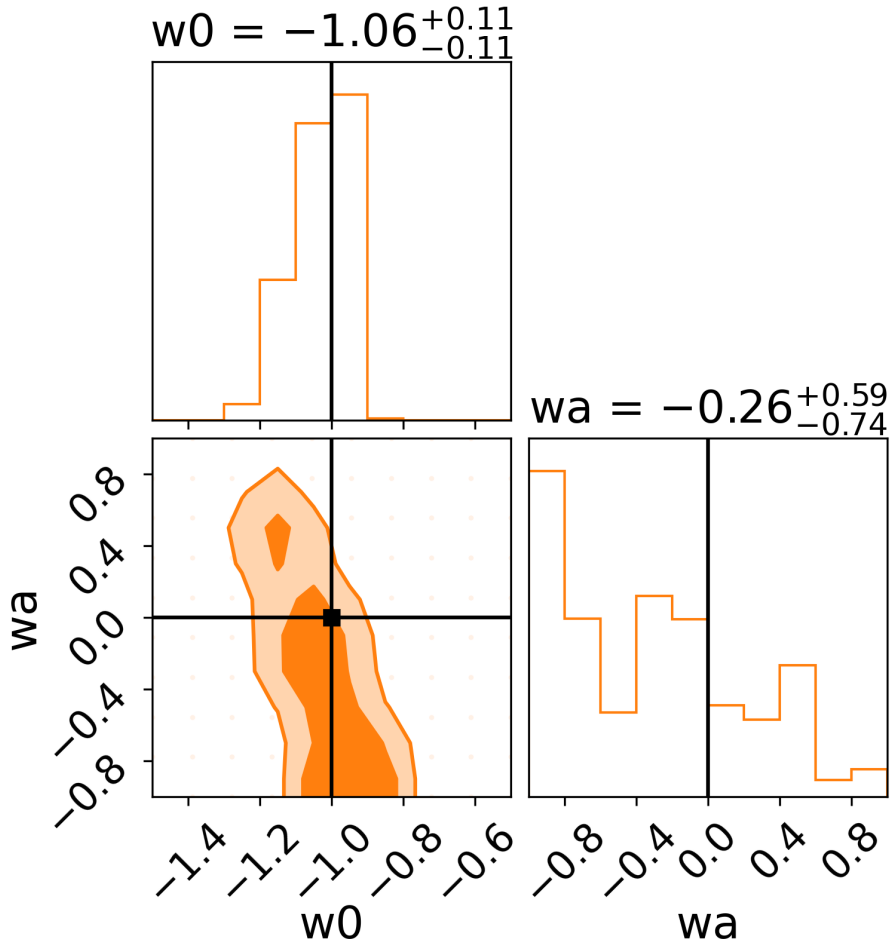

Figure 4.4: *Joint posterior constraints on (w_0, w_a) from the `FID` simulation using narrow priors, obtained by combining the $z = 0.5$ and $z = 0.7$ redshift shells ($\Delta z = 0.1$). Contours show the 68% and 95% confidence regions.w_0 is well constrained but w_a is poorly constrained. The black lines indicate the true cosmology. The true values of w_0 and w_a of the fiducial cosmology fall within the 68% confidence contour. $N_{realisations} = 6$*

Version of February 12, 2026– Created February 12, 2026 - 20:24

4.3.2 Priors

Two prior choices are used for the $w_0 w_a$CDM analyses that follow from this point forward. Unless stated otherwise in the caption of a figure, results labelled **narrow priors** adopt

$$w_0^{\text{narrow}} \sim U[-1.5, -0.5] \qquad w_a^{\text{narrow}} \sim U[-1, 1]$$

while results labelled **DESI priors** use broader uniform ranges following the DESI analysis strategy [8],

$$w_0^{\text{DESI}} \sim U[-3, 1] \qquad w_a^{\text{DESI}} \sim U[-3, 2]$$

For all two parameter (w_0, w_a) posterior evaluations shown in the `corner.corner` plots, the likelihood is evaluated on a uniform grid of 30×30 points spanning the chosen prior ranges (including both endpoints). This corresponds to step sizes:

$$\Delta w_0^{\text{narrow}} = \frac{-0.5 - (-1.5)}{30 - 1} = \frac{1}{29} \simeq 0.034 \quad \Delta w_a^{\text{narrow}} = \frac{1 - (-1)}{30 - 1} = \frac{2}{29} \simeq 0.069$$

$$\Delta w_0^{\text{DESI}} = \frac{1 - (-3)}{30 - 1} = \frac{4}{29} \simeq 0.138 \qquad \Delta w_a^{\text{DESI}} = \frac{2 - (-3)}{30 - 1} = \frac{5}{29} \simeq 0.172$$

Version of February 12, 2026– Created February 12, 2026 - 20:24

4.3.3 WOWA: narrow priors

Validation of WOWA simulation at $z = 0.5$

The same validation procedure is done as in section 4.3.3 to verify if the BAO is fitted correctly in the WOWA simulation for the correct cosmology.

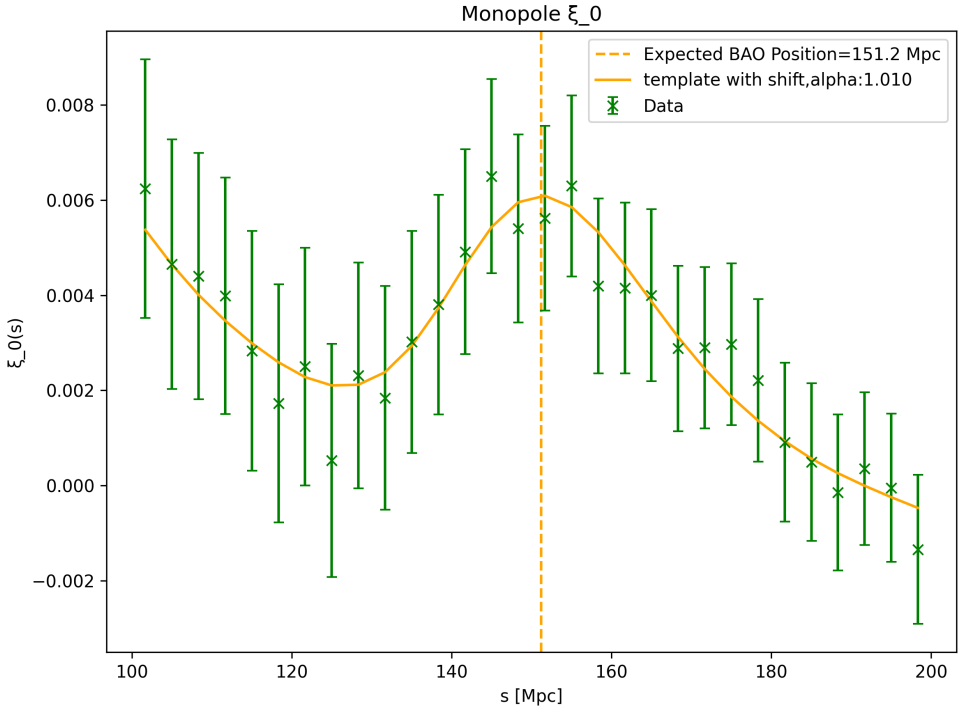

Figure 4.5: *Monopole BAO fit for the WOWA simulation (narrow priors) with the correct cosmological values for (w_0, w_a) at $z = 0.5$. The vertical dotted line indicates the expected BAO peak position in comoving separation (Mpc) for the fiducial template. The green data points with error bars show the measured monopole correlation function $\xi_0^{\text{data}}(s)$, while the yellow curve shows the best-fitting shifted template model $\xi_0^{\text{model}}(s)$ obtained by minimizing the χ^2 defined in Eq. 3.26. The best-fitting dilation parameter is $\alpha = 1.01$ (no σ_α shown, error is computed internally). $N_{realisations} = 6$.*

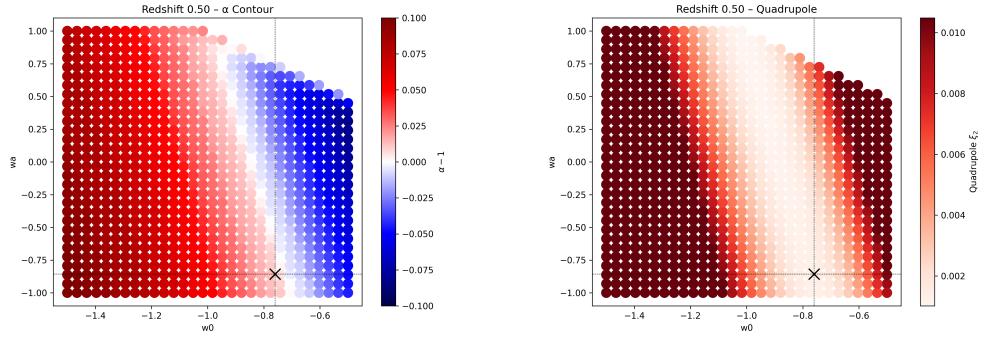

(a) ***(b)***

Figure 4.6: *Left: BAO dilation parameter shift α for the* `WOWA` *simulation with narrow priors at redshift $z = 0.5$, evaluated using Eq. 3.26. Red regions indicate BAO scales larger than the fiducial template, while blue regions correspond to smaller inferred BAO scales. The cross marks the true simulation cosmology and lies close to $\alpha = 1$, indicating good overall recovery. Right: Average quadrupole $\langle \xi_2 \rangle$ measured over separations* 100–200 Mpc *as in Eq. 3.28 for the same configuration. The quadrupole remains consistent with zero within uncertainties, with the true cosmology (cross) being among the cosmologies with the lowest anisotropy. For both quadrupole and α plots we see some points (especially in the top right corner) are blank. This means the pipeline was not able to recover a correct fit for that cosmology. $N_{realisations} = 6$.*

Combined redshift shells at $z = 0.5$ and $z = 0.7$

Fig. 4.7 shows the posterior distribution of the dark energy equation-of-state parameters (w_0, w_a) obtained from a joint likelihood analysis combining the redshift shells centered at $z = 0.5$ and $z = 0.7$, each with a bin width of $\Delta z = 0.1$, corresponding to the intervals $0.45 \leq z \leq 0.55$ and $0.65 \leq z \leq 0.75$. The posterior is visualized using a two-parameter `corner.corner` plot, where the contours represent the marginalized constraints in the (w_0, w_a) plane.
Marginalizing over w_a and w_0 respectively yield the following constraints

$$\begin{aligned} w_0 &= -0.84^{+0.10}_{-0.10} \quad (68\%\ \text{CI}) \\ w_a &= -0.38^{+0.69}_{-0.48} \quad (68\%\ \text{CI}) \end{aligned} \tag{4.3}$$

The resulting confidence region is highly elongated, indicating a strong degeneracy between w_0 and w_a when only the lower redshift information is used.

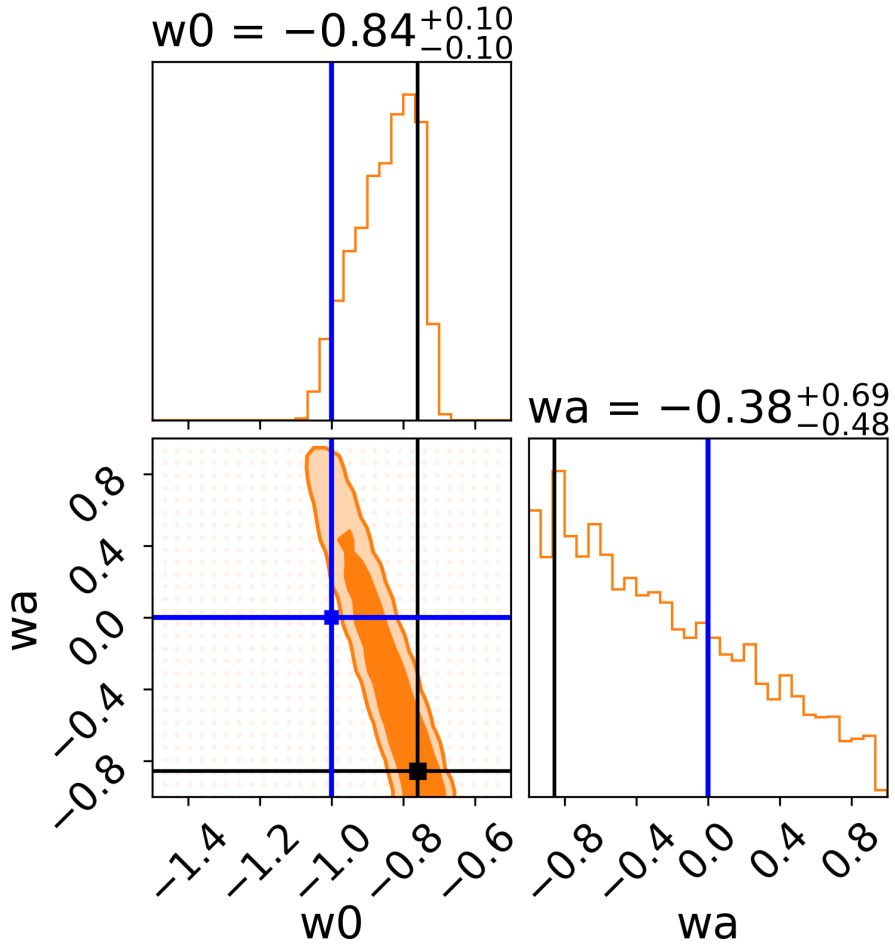

Figure 4.7: *Joint posterior constraints on (w_0, w_a) from the* `WOWA` *simulation using narrow priors, obtained by combining the $z = 0.5$ and $z = 0.7$ redshift shells ($\Delta z = 0.1$). Contours show the 68% and 95% confidence regions. The black lines indicate the true values of the simulations and the blue lines indicate the* `FID` *cosmological constant simulation values. Contours show the 68% and 95% confidence regions. $N_{realisations} = 10$.*

Including higher redshift information

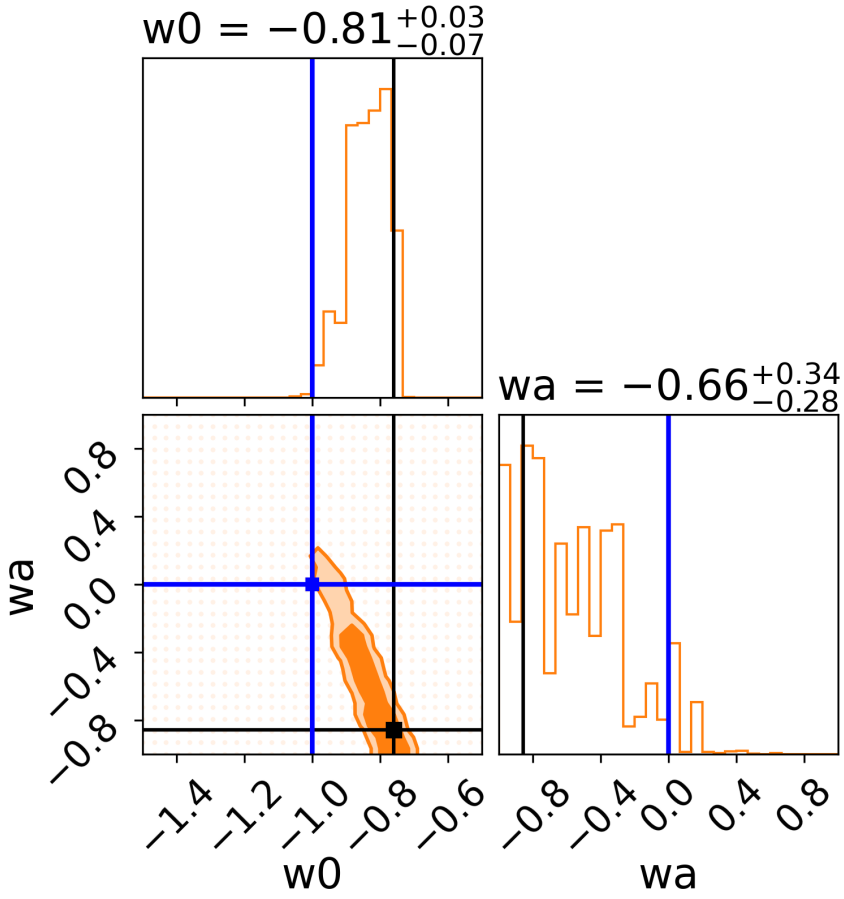

Figure 4.8: *Joint posterior constraints on (w_0, w_a) from the* `WOWA` *simulation using narrow priors, combining the $z = 0.5$, $z = 0.7$, and $z = 0.9$ redshift shells. Contours show the 68% and 95% confidence regions. The black lines indicate the true values of the simulations and the blue lines indicate the* `FID` *cosmological constant simulation values. Including the higher-redshift bin partially breaks the (w_0, w_a) degeneracy and tightens the confidence contours, although the low tracer abundance at $z = 0.9$ makes BAO recovery less stable in that shell. $N_{realisations} = 10$.*

To investigate whether this degeneracy can be reduced, an additional higher redshift shell at $z = 0.9$ is included in the analysis. The resulting posterior distribution is shown in Fig. 4.8, where the combined likelihood now incorporates the redshift shells at $z = 0.5$, $z = 0.7$, and $z = 0.9$. In this case, the confidence contours are noticeably more compact and are more tightly centered around the true parameter values $(w_0, w_a) = (-0.760, -0.857)$

Version of February 12, 2026– Created February 12, 2026 - 20:24

used in the simulation and the FID cosmology is just outside the 95% confidence interval. However, this redshift bin galaxy count is low (≈ 6000) and this means the BAO signal cannot be resolved in a few of the runs. This is the reason why this redshift bin has been ejected from further analysis. A larger simulation would make this redshift bin more viable to include in the final posterior and constrain the (w_0, w_a) values even better. For this configuration, the marginalized constraints improve to

$$\begin{aligned} w_0 &= -0.81^{+0.03}_{-0.07} \quad (68\%\ \text{CI}) \\ w_a &= -0.66^{+0.34}_{-0.28} \quad (68\%\ \text{CI}) \end{aligned} \tag{4.4}$$

This demonstrates that including higher-redshift information helps to partially break the degeneracy between w_0 and w_a, leading to tighter constraints on both parameters.

Effect of prior choice

However, for both Fig. 4.7 and Fig. 4.8, the confidence intervals visibly extend to regions outside the imposed priors. This suggests that the chosen prior ranges may be overly restrictive and could artificially truncate the posterior distribution.

To address this issue, a third analysis is performed using wider priors consistent with those adopted in the DESI analysis.[8] This new analysis allows the full extent of the likelihood surface to be explored without prior induced boundary effects and provides a more fair assessment of the cosmological constraints.

Version of February 12, 2026– Created February 12, 2026 - 20:24

4.3.4 `FID`: DESI priors

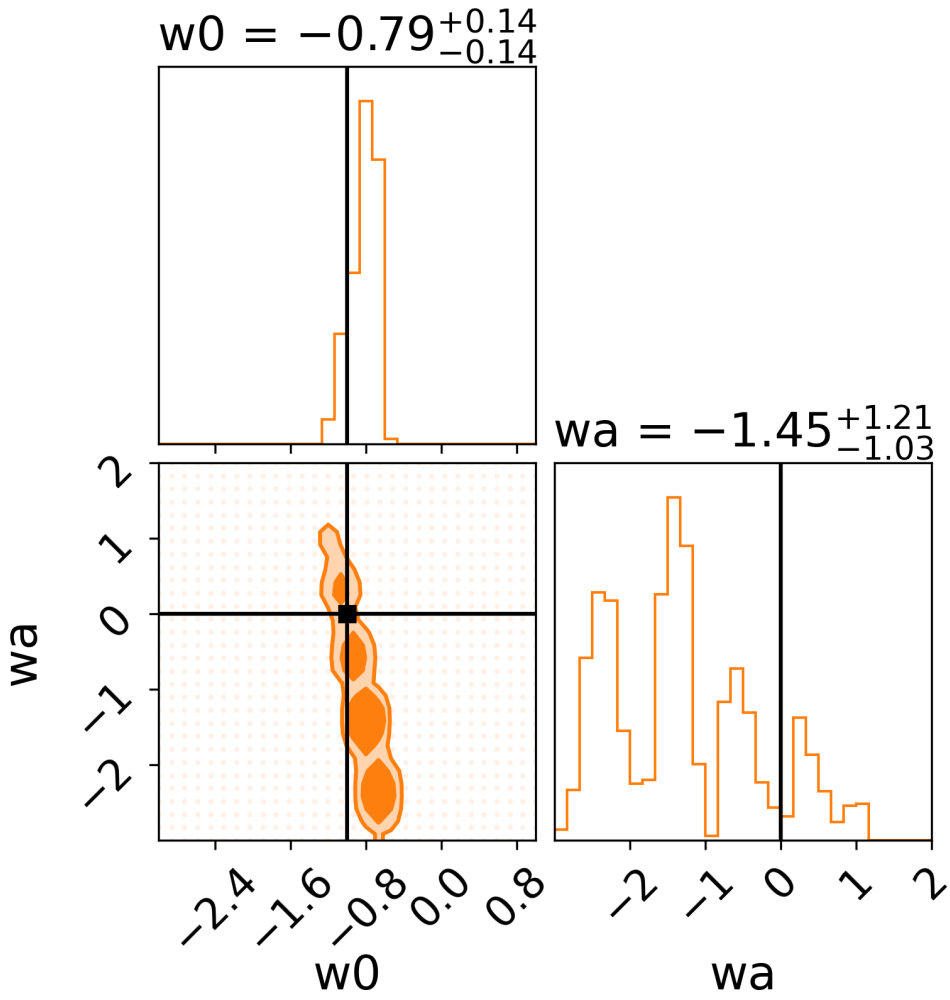

Figure 4.9: *Joint posterior constraints on (w_0, w_a) from the `FID` simulation using DESI priors, obtained by combining the $z = 0.5$ and $z = 0.7$ redshift shells. Relative to the narrow-prior case, the wider prior range reveals the full extent of the (w_0, w_a) degeneracy and leads to weaker marginal constraints. Contours show the 68% and 95% confidence regions. The true cosmology is indicated with black lines. When compared to Fig. 4.4 the w_0 value is less well constrained and lies further away from the true value of $w_0 = -1$. w_a is again poorly constrained. $N_{realisations} = 6$.*

Version of February 12, 2026– Created February 12, 2026 - 20:24

When adopting the wider DESI prior ranges, the resulting constraints on the dark energy equation-of-state parameters seen in 4.5 and in Fig. 4.9 become significantly weaker compared to those obtained with the narrow priors in 4.2. In particular, the marginalised uncertainty on w_0 increases, while the constraint on w_a remains effectively unconstrained, reflecting the strong degeneracy between the two parameters when limited redshift information is available.

Although the best-fitting value of w_0 lies approximately 1.5σ away from the cosmological constant value $w_0 = -1$, this level of deviation is not statistically significant enough to say the pipeline failed to recover the true cosmology. The `FID` cosmology still falls within the 95 % confidence interval. It does show that the prior choice has a big influence on the resulting posterior and w_0 marginal.

$$\begin{aligned} w_0 &= -0.79^{+0.14}_{-0.14} \quad (68\%\ \mathrm{CI}) \\ w_a &= -1.45^{+1.21}_{-1.03} \quad (68\%\ \mathrm{CI}) \end{aligned} \tag{4.5}$$

Version of February 12, 2026– Created February 12, 2026 - 20:24

4.3.5 WOWA: DESI priors

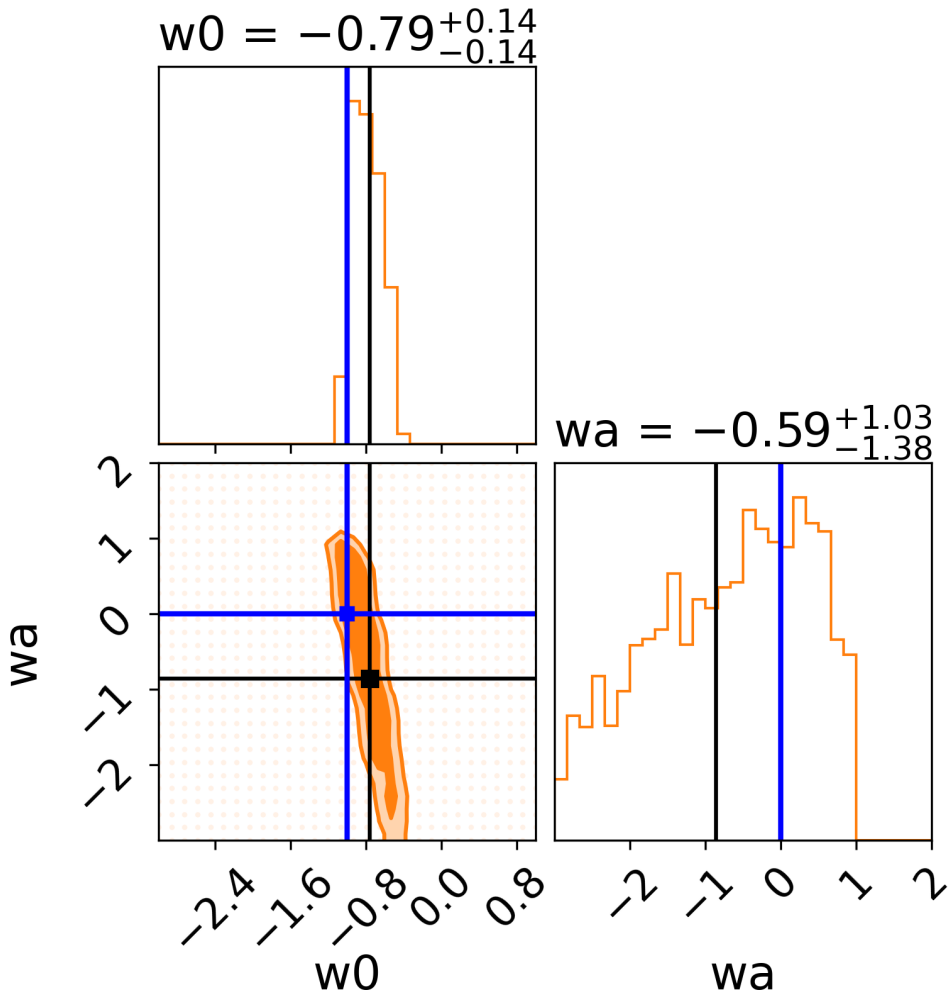

Figure 4.10: *Joint posterior constraints on (w_0, w_a) from the WOWA simulation using DESI priors, obtained by combining the $z = 0.5$ and $z = 0.7$ redshift shells. Contours show the 68% and 95% confidence regions. The black lines indicate the true values of the simulations and the blue lines indicate the FID cosmological constant simulation values. Relative to the narrow-prior case, the wider prior range reveals the full extent of the (w_0, w_a) degeneracy and leads to weaker marginal constraints. $N_{realisations} = 5$ (one corrupted realisation).*

Version of February 12, 2026– Created February 12, 2026 - 20:24

When adopting the wider DESI prior ranges, the resulting constraints on the dark energy equation-of-state parameters become significantly weaker compared to those obtained with the narrow priors in 4.3. In particular, the marginalised uncertainty on w_0 increases substantially, while the constraint on w_a remains effectively unconstrained, reflecting the strong degeneracy between the two parameters when limited redshift information is available. Although the best-fitting value of w_0 lies approximately 1.5σ away from the cosmological constant value $w_0 = -1$, this level of deviation is not statistically significant.

Consequently, it remains premature to claim a confident distinction between the evolving w_0w_aCDM cosmology considered here and a standard ΛCDM model based on the current analysis. The resulting posterior contours in Fig. 4.10 are indistinguishable from the `FID` simulation in Fig. 4.9.

$$\begin{aligned} w_0 &= -0.79^{+0.14}_{-0.14} \quad (68\%\ \text{CI}) \\ w_a &= -0.59^{+1.03}_{-1.38} \quad (68\%\ \text{CI}) \end{aligned} \tag{4.6}$$

Version of February 12, 2026– Created February 12, 2026 - 20:24

4.3.6 `WOWA+AGN`: DESI priors

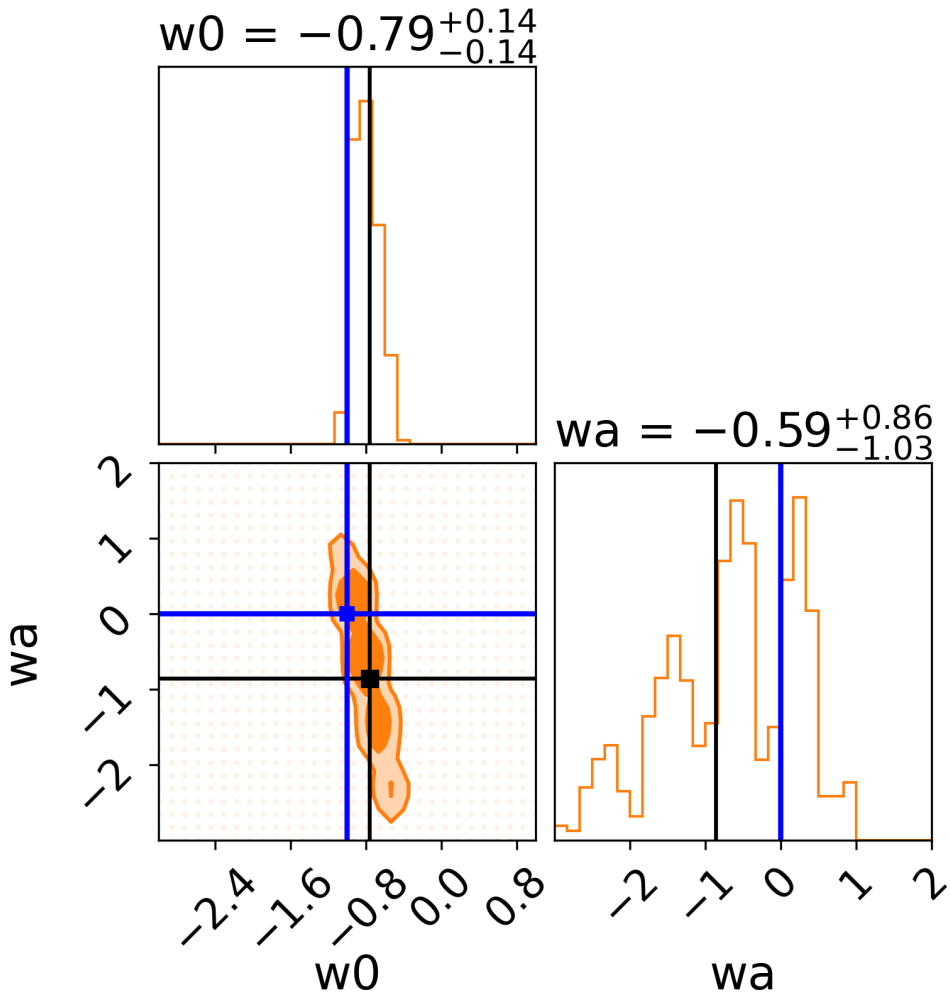

Figure 4.11: *Joint posterior constraints on (w_0, w_a) from the `WOWA+AGN` simulation using DESI priors, combining the $z = 0.5$ and $z = 0.7$ redshift shells. Contours show the 68% and 95% confidence regions. The black lines indicate the true values of the simulations and the blue lines indicate the `FID` cosmological constant simulation values. The higher tracer density in this run yields a tighter constraint on w_0 compared to `WOWA`, while w_a remains weakly constrained due to the persistent (w_0, w_a) degeneracy at these redshifts. $N_{realisations} = 6$.*

Version of February 12, 2026– Created February 12, 2026 - 20:24

The properties of the `WOWA+AGN` simulation help to explain the constraining power of the resulting posterior. As shown in table 4.1, this run exhibits a higher LRG tracer number density compared to the corresponding models with weaker AGN feedback. This enhancement arises because the inclusion of strong AGN feedback leads to earlier quenching of star formation in massive galaxies, producing a larger population of passively evolving red galaxies at earlier cosmic times. Such early quenching is a key ingredient in boosting the abundance of luminous red galaxies at higher redshifts. [44]

The increased tracer density improves the signal-to-noise of the clustering measurements in both redshift bins as can be seen in table 4.1. This contributes to the tighter marginal constraint on w_0 shown in Fig. 4.11. We find that the ΛCDM value $w_0 = -1$ remains well within the 1σ confidence interval of the marginalised posterior, indicating no statistically significant deviation from a cosmological constant. In contrast, the time variation parameter w_a remains weakly constrained, reflecting the limited sensitivity of the current data combination to a deviation from constant dark energy at these redshifts. The resulting posterior contours in Fig. 4.11 are indistinguishable from the `FID` simulation in Fig. 4.9.

$$\begin{aligned} w_0 &= -0.79^{+0.14}_{-0.14} \quad (68\%\ \text{CI}) \\ w_a &= -0.59^{+0.86}_{-1.03} \quad (68\%\ \text{CI}) \end{aligned} \tag{4.7}$$

Version of February 12, 2026– Created February 12, 2026 - 20:24

4.4 Fixing w_0

This section investigates whether fixing w_0 at its corresponding true simulation improves constraints on w_a and furthermore can distinghuish dynamical dark energy from cosmological constant simulations. The analysis is performed for all three simulations considered above. When analysing the posterior contours, the `WOWA` and `WOWA+AGN` simulations are indistinguishable from the `FID` simulation. There is not enough information to show that the `WOWA` and `WOWA+AGN` simulation are run with a dynamical dark energy model instead of the standard cosmological constant.

When fixing w_0 and varying only w_a, the likelihood is evaluated on a one-dimensional uniform grid of 300 points across the DESI prior range $w_a \sim U[-3, 2]$ (including endpoints). The corresponding spacing is

$$\Delta w_a^{\mathrm{DESI}} = \frac{2-(-3)}{300-1} = \frac{5}{299} \simeq 0.017. \tag{4.8}$$

4.4.1 FID

These results correspond to the DESI prior w_a only analysis of the FID simulation, in which the true cosmology is ΛCDM with $w_a = 0$. As shown in Fig. 4.14a and Fig. 4.12b, the posteriors inferred from the individual redshift shells at $z = 0.5$ and $z = 0.7$ are noticeably offset from one another, indicating a substantial redshift dependence of the recovered w_a value even in the absence of dynamical dark energy inside the simulation.

Quantitatively, the $z = 0.5$ shell prefers a mildly positive value of w_a, while the $z = 0.7$ shell favours a negative value, leading to a mild tension between the two measurements. This behaviour closely mirrors the pattern observed in the WOWA simulation and reflects the limited constraining power of a single BAO redshift shell on the time variation of the dark energy equation of state.

When the two shells are combined, the resulting posterior shown in Fig. 4.13 peaks close to the true value $w_a = 0$ and remains consistent with ΛCDM at the $\sim 1\sigma$ level. This demonstrates that, despite significant disagreement between individual redshift bins, the combined constraint does not falsely indicate dynamical dark energy in the fiducial cosmological constant simulation.

$$\begin{aligned} w_{a,z=0.5} &= 0.41^{+0.31}_{-0.37} \quad (68\%\ \mathrm{CI}) \\ w_{a,z=0.7} &= -0.98^{+0.23}_{-0.45} \quad (68\%\ \mathrm{CI}) \\ w_{a,\mathrm{combined}} &= -0.28^{+0.20}_{-0.20} \quad (68\%\ \mathrm{CI}) \end{aligned} \tag{4.9}$$

Version of February 12, 2026– Created February 12, 2026 - 20:24

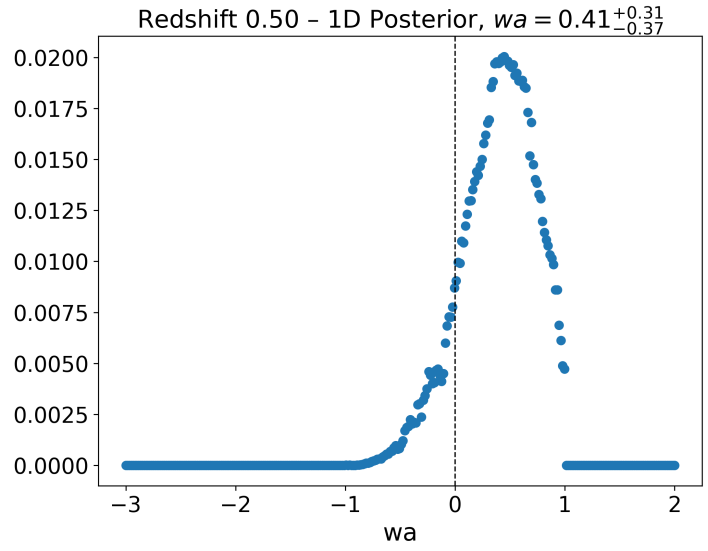

(a) $z = 0.5$

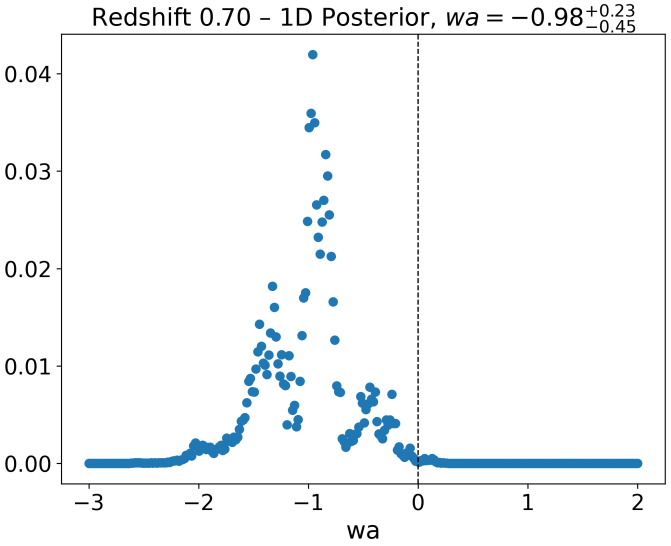

(b) $z = 0.7$

Figure 4.12: *One-dimensional posteriors for the dark energy time-variation parameter w_a obtained from the `FID` simulation using DESI priors, shown separately for the redshift shells at $z = 0.5$ (top) and $z = 0.7$ (bottom). The two shells favour different values of w_a, indicating a strong redshift dependence of the inferred constraint when w_0 is fixed. The true cosmology is indicated with the vertical black dotted line. $N_{realisations} = 6$.*

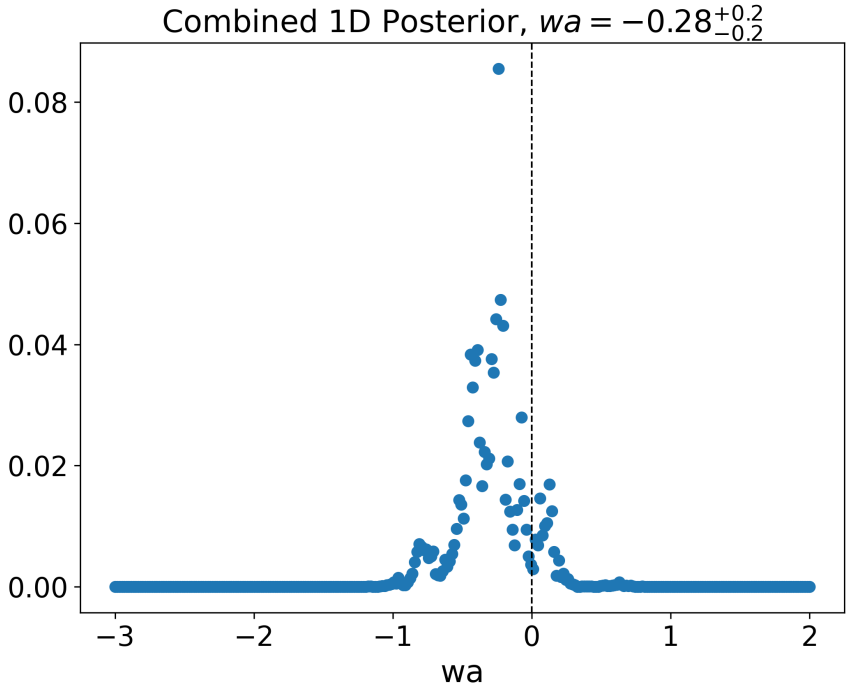

Figure 4.13: *Combined posterior distribution for w_a from the `FID` simulation, obtained by multiplying the likelihoods from the $z = 0.5$ and $z = 0.7$ redshift shells under the assumption of independent measurements. The resulting constraint peaks close to the true value $w_a = 0$ and remains consistent with ΛCDM at the $\sim 1\sigma$ level, despite the tension between the individual redshift bin posteriors. The true cosmology is indicated with the vertical black dotted line. $N_{realisations} = 6$.*

4.4.2 WOWA

These results correspond to the DESI-prior w_a only analysis of the WOWA simulation, with the marginalized constraints summarized in 4.10. As shown in Fig. 4.14a and Fig. 4.14b, there is a clear discrepancy between the posterior distributions inferred from the individual redshift shells at $z = 0.5$ and $z = 0.7$, indicating that the recovered value of w_a is strongly dependent on the redshift range considered. This highlights difficulty of constraining the time variation of the dark energy equation of state once again, even when w_0 and all other cosmological parameters are held fixed.

When the two redshift shells are combined, the resulting posterior shown in Fig. 4.15 yields a constraint on w_a that lies more than 4σ away from the ΛCDM value $w_a = 0$. However, given the significant tension between the individual redshift posteriors, it remains premature to interpret this deviation as conclusive evidence for a departure from ΛCDM. While the posteriors derived from the individual redshift shells at $z = 0.5$ and $z = 0.7$ (Figs. 4.14a and 4.14b) exhibit approximately Gaussian shapes, the combined posterior shows no clear or well-defined Gaussian structure. This disparity might have something to do with with the assumption that the likelihoods of the two shells are independent as in Eq. 3.8.

$$\begin{aligned} w_{a,z=0.5} &= -1.7^{+0.22}_{-0.2} \quad (68\%\ \text{CI}) \\ w_{a,z=0.7} &= -0.46^{+0.29}_{-0.3} \quad (68\%\ \text{CI}) \\ w_{a,combined} &= -1.3^{+0.26}_{-0.23} \quad (68\%\ \text{CI}) \end{aligned} \tag{4.10}$$

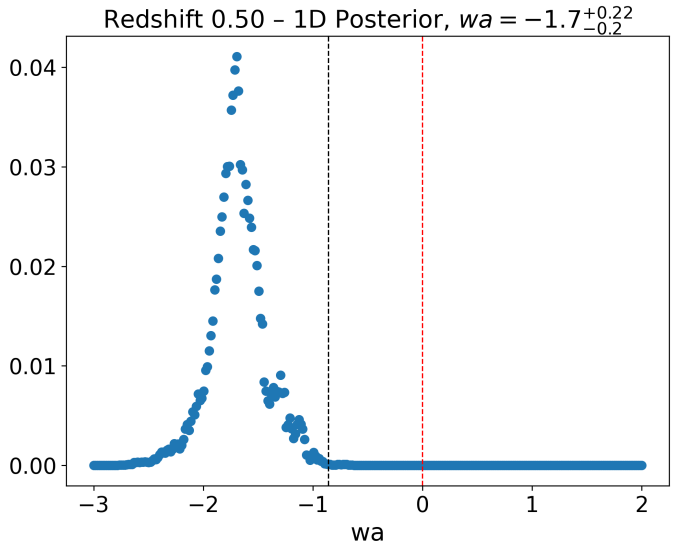

(a) $z = 0.5$

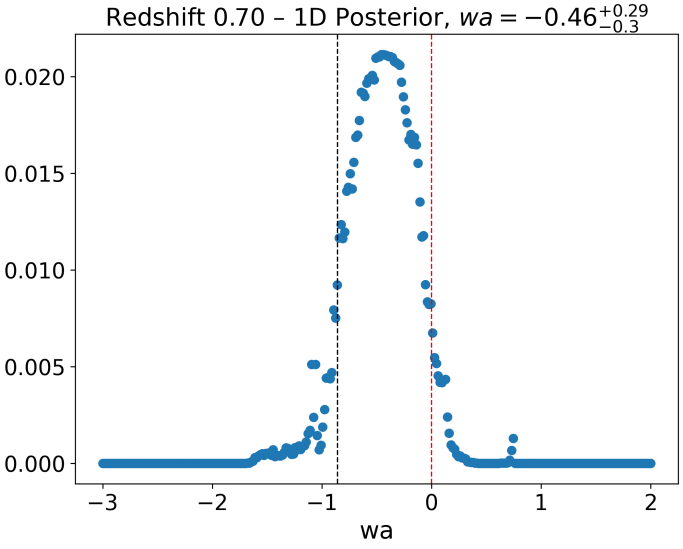

(b) $z = 0.7$

Figure 4.14: *One-dimensional posteriors for the dark energy time-variation parameter w_a obtained from the* `WOWA` *simulation using DESI priors, shown separately for the redshift shells at $z = 0.5$ and $z = 0.7$. The true cosmology is indicated with the vertical black dotted line and the* `FID` *cosmology is indicated with a red dotted line. The two redshift bins favour substantially different values of w_a, with minimal overlap between the posteriors, indicating strong redshift dependent variation when w_0 is held fixed. $N_{realisations} = 6$.*

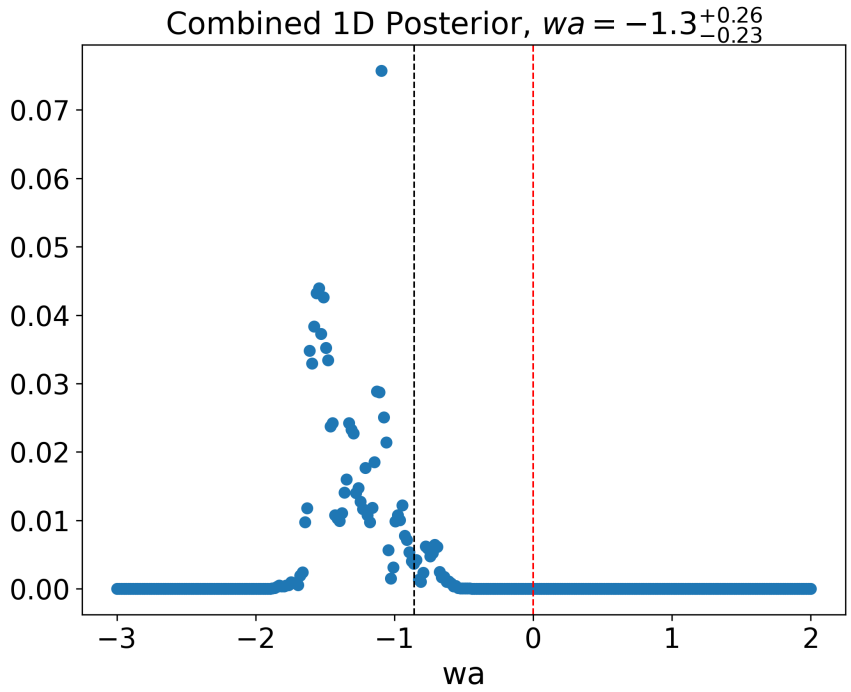

Figure 4.15: *Combined posterior distribution for w_a from the* `WOWA` *simulation, obtained by combining the likelihoods from the $z = 0.5$ and $z = 0.7$ redshift shells under the assumption of independent measurements. The true cosmology is indicated with the vertical black dotted line and the* `FID` *cosmology is indicated with a red dotted line. The resulting constraint lies more than 4σ away from the ΛCDM value $w_a = 0$ and approximately 2σ away from the true simulation value of $w_a = -0.857$. $N_{realisations} = 6$.*

Version of February 12, 2026– Created February 12, 2026 - 20:24

4.4.3 WOWA+AGN

The WOWA+AGN simulation exhibits qualitatively different behaviour compared to both the FID and WOWA runs. As shown in Fig. 4.16a and Fig. 4.16b, the posteriors obtained from the individual redshift shells at $z = 0.5$ and $z = 0.7$ are in substantially better agreement with one another and are both centred close to the true simulation value of w_a.

This improved consistency is also reflected in the combined posterior (Fig. 4.17), which remains well centred around the true $w_a = -0.857$ value and shows a comparatively narrower width than the corresponding WOWA case. The agreement between the two redshift bins suggests that, for this simulation, systematic redshift dependence in the recovered w_a is significantly reduced.

A plausible explanation for this behaviour is the higher luminous red galaxy tracer density in the WOWA+AGN run, particularly at $z \gtrsim 0.5$, as shown in Table 4.2. The enhanced tracer abundance increases the SNR of the BAO measurement and reduces Poisson noise in the two-point correlation function, leading to more stable w_a inference across redshift bins.

$$\begin{aligned} w_{a,z=0.5} &= -0.87^{+0.27}_{-0.42} \quad (68\%\ \text{CI}) \\ w_{a,z=0.7} &= -1.30^{+0.74}_{-0.70} \quad (68\%\ \text{CI}) \\ w_{a,\text{combined}} &= -0.91^{+0.24}_{-0.40} \quad (68\%\ \text{CI}) \end{aligned} \tag{4.11}$$

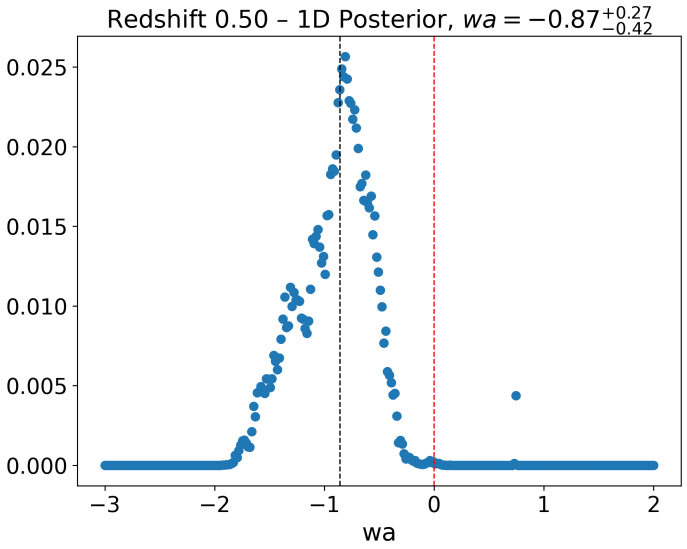

(a) $z = 0.5$

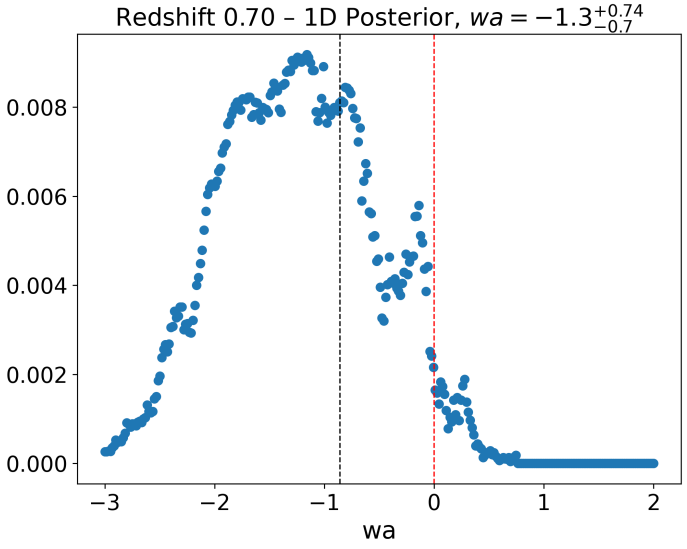

(b) $z = 0.7$

Figure 4.16: *One-dimensional posteriors for the dark energy time-variation parameter w_a obtained from the `WOWA+AGN` simulation using DESI priors, shown separately for the redshift shells at $z = 0.5$ and $z = 0.7$. The true cosmology is indicated with the vertical black dotted line and the `FID` cosmology is indicated with a red dotted line. In contrast to the `FID` and `WOWA` runs, the two posteriors are in good agreement and are both centred close to the true simulation value of $w_a = -0.857$, indicating reduced redshift-dependent systematics. $N_{realisations} = 6$.*

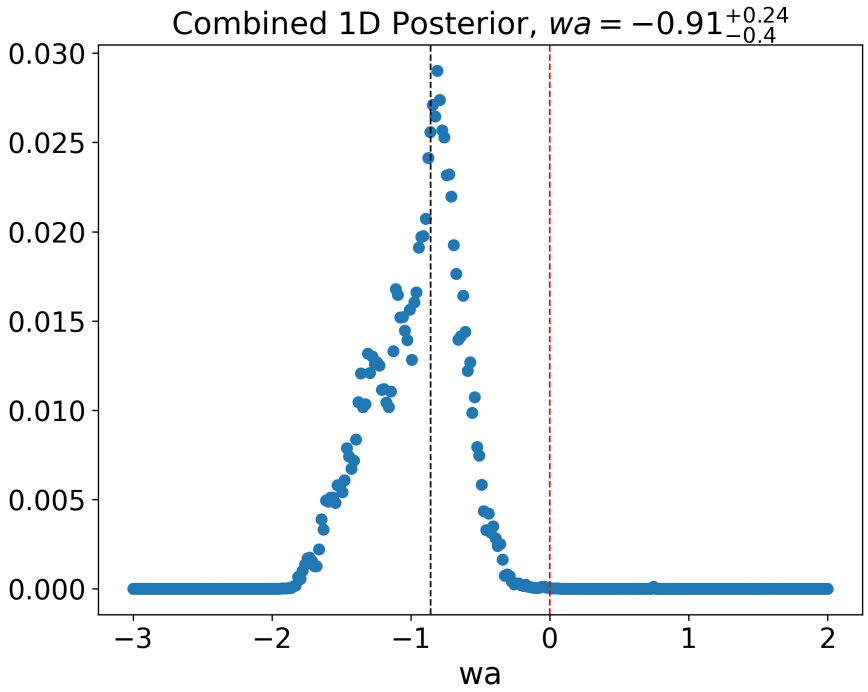

Figure 4.17: *Combined posterior distribution for w_a from the `WOWA+AGN` simulation, obtained by combining the likelihoods from the $z = 0.5$ and $z = 0.7$ redshift shells under the assumption of independent measurements. The true cosmology is indicated with the vertical black dotted line and the `FID` cosmology is indicated with a red dotted line. The resulting constraint is well centred around the true value $w_a = -0.857$ and is narrower than in the corresponding `WOWA` case. The ΛCDM value $w_a = 0$ lies approximately 3–4σ away from the posterior maximum. $N_{realisations} = 6$.*

Version of February 12, 2026– Created February 12, 2026 - 20:24

4.5 Overview

Table 4.2: *Summary of dark energy parameter constraints from the FLAMINGO* `L1000N1800` *simulations. All quoted uncertainties correspond to 68% confidence intervals. For the w_a–only analyses, w_0 is held fixed at its true simulation value just like the rest of the cosmological parameters.*

Simulation	**Analysis (z shells used)**	**Priors**	w_0 **(68% CI)**	w_a **(68% CI)**
`FID`	w_0–w_a $(0.5, 0.7)$	narrow	$-1.06^{+0.11}_{-0.11}$	$-0.26^{+0.59}_{-0.74}$
`WOWA`	w_0–w_a $(0.5, 0.7)$	Narrow	$-0.84^{+0.10}_{-0.10}$	$-0.38^{+0.69}_{-0.48}$
`WOWA`	w_0–w_a $(0.5, 0.7, 0.9)$	Narrow	$-0.81^{+0.03}_{-0.07}$	$-0.66^{+0.34}_{-0.28}$
`FID`	w_0–w_a $(0.5, 0.7)$	DESI	$-0.79^{+0.14}_{-0.14}$	$-1.45^{+1.21}_{-1.03}$
`WOWA`	w_0–w_a $(0.5, 0.7)$	DESI	$-0.79^{+0.28}_{-0.14}$	$-0.59^{+1.03}_{-1.38}$
`WOWA+AGN`	w_0–w_a $(0.5, 0.7)$	DESI	$-0.79^{+0.14}_{-0.14}$	$-0.59^{+0.86}_{-1.03}$
`FID`	w_a (0.5)	DESI	fixed	$0.41^{+0.31}_{-0.37}$
`FID`	w_a (0.7)	DESI	fixed	$-0.98^{+0.23}_{-0.45}$
`FID`	w_a $(0.5, 0.7)$	DESI	fixed	$-0.28^{+0.2}_{-0.2}$
`WOWA`	w_a (0.5)	DESI	fixed	$-1.70^{+0.22}_{-0.20}$
`WOWA`	w_a (0.7)	DESI	fixed	$-0.46^{+0.29}_{-0.30}$
`WOWA`	w_a $(0.5, 0.7)$	DESI	fixed	$-1.30^{+0.26}_{-0.23}$
`WOWA+AGN`	w_a (0.5)	DESI	fixed	$-0.87^{+0.27}_{-0.42}$
`WOWA+AGN`	w_a (0.7)	DESI	fixed	$-1.3^{+0.74}_{-0.7}$
`WOWA+AGN`	w_a $(0.5, 0.7)$	DESI	fixed	$-0.91^{+0.24}_{-0.4}$

Version of February 12, 2026– Created February 12, 2026 - 20:24

Chapter 5

Discussion and conclusion

This thesis developed and applied an end-to-end BAO analysis pipeline to DESI-like luminous red galaxy (LRG) mock catalogues constructed from the FLAMINGO hydrodynamical simulations. The goal was to test whether BAO measurements in a hydrodynamical simulation can (i) recover the correct cosmology when analysed under the true model, and (ii) recover dynamical dark energy parameters in a $w_0 w_a$CDM simulation in a way that is qualitatively consistent with current survey analyses. The physical motivation is that BAO are set by early universe photon–baryon physics and the drag-epoch sound horizon [1–4], while late time non-linearities and baryonic processes primarily affect the broadband shape rather than the BAO peak position.[5]

DESI is now measuring BAO with high precision and has reported constraints on (w_0, w_a) that motivate validation of these results within simulations such as FLAMINGO.[8–10]

Version of February 12, 2026– Created February 12, 2026 - 20:24

5.1 Key results

5.1.1 BAO scale recovery

A baseline validation is that analysing a snapshot under the correct cosmological parameters should yield $\alpha \simeq 1$ from the monopole BAO fit (Eq. 3.26). For the `W0WA` simulation at $z = 0.5$, the monopole template fit reproduces the observed BAO feature well (Fig. 4.5), and the true (w_0, w_a) location lies close to $\alpha = 1$ in the α-map (Fig. 4.6). The quadrupole diagnostic, defined by the averaged $\langle \xi_2 \rangle$ statistic (Eq. 3.28), remains consistent with zero near the true cosmology (Fig. 4.6), supporting the interpretation that no significant anisotropic distortion is present in this configuration, consistent with the geometric arguments in Sec. 2.2.1.[20]

5.1.2 Detecting a non-ΛCDM cosmology

Under the assumption of narrow (w_0, w_a) priors, the combined posterior for the `W0WA` simulation is statistically distinct from that of the `FID` simulation, allowing the two cosmologies to be distinguished in the w_0–w_a plane. In this case, the ΛCDM point lies within the 68% confidence region for `FID` as can be seen in Fig. 4.4, but outside the 95% confidence region for `W0WA` as can be seen in Fig. 4.7.

However, when we change to DESI priors on (w_0, w_a) the resulting posteriors of `FID`,`W0WA` and `W0WA+AGN` are almost indistinguishable. This can be seen by comparing Figs. 4.9, 4.10 and 4.11 respectively. This might be due to the larger Δw_a and Δw_0 compared to the narrow (w_0, w_a) priors and the rudimentary way of taking a uniform 2 dimensional grid inside the (w_0, w_a) DESI priors that causes the pipeline to not sample the high probability cosmologies often enough. This can be solved by implementing a Markov chain Monte Carlo (MCMC) algorithm that selects (w_0, w_a) combinations in a way that samples the higher probability regions more closely.[45]

Version of February 12, 2026– Created February 12, 2026 - 20:24

Including a higher redshift shell at $z = 0.9$ can, in the case of the `WOWA` simulation (with narrow (w_0, w_a) priors), occasionally yield a clearer separation from ΛCDM as seen in Fig. 4.8. This is consistent with the fact that including higher redshift measurements samples a larger fraction of the redshift evolution of $w(z)$ (Eq. 3.4), thereby providing increased leverage on time variation in the dark energy equation of state. In practice, however, the low tracer count (≈ 6000) in this shell leads to reduced BAO signal-to-noise and a fragile fitting procedure, limiting the robustness of this detection and the choice of excluding it from the final inference for now.

Fixing w_0

When keeping w_0 fixed and fitting only w_a, the resulting constraints differ qualitatively between the three simulations. For the `FID` simulation, fixing $w_0 = -1$ yields a posterior that is consistent with the cosmological constant value $w_a = 0$ within approximately 1.5σ (Fig. 4.13), indicating that static dark energy cannot be ruled out in this case and the pipeline works.

In contrast, for the `WOWA` and `WOWA+AGN` simulations, where w_0 is fixed to the true input value $w_0 = -0.760$, the inferred values of w_a show a clear and statistically significant deviation from $w_a = 0$. The `WOWA` simulation exhibits a $\sim 5\sigma$ deviation from the cosmological constant case and lies at a level of $\gtrsim 1.5\sigma$ from the true simulation value $w_a = -0.857$ (Fig.4.15). The `WOWA+AGN` simulation shows a $\sim 4\sigma$ deviation from $w_a = 0$, with the inferred mean value lying within 1σ of the true input $w_a = -0.857$ (Fig.4.17).

It is important to note that, for the `WOWA` and `WOWA+AGN` simulations, fixing w_0 at its true value already encodes prior information that the cosmology is not ΛCDM. Within this controlled setting, the analysis nevertheless demonstrates that w_a is robustly non-zero in both simulations, implying genuinely dynamical dark energy. By contrast, for the `FID` simulation, no such conclusion can be drawn, and ΛCDM with $w_a = 0$ remains fully consistent with the data.

5.2 Limitations

Across snapshots, the recovered α values for the true cosmologies are typically close to unity but show a mild tendency towards $\alpha < 1$ at higher redshift. A one-sided preference for $\alpha < 1$ (rather than symmetric scatter about unity) suggests that the effect is not purely statistical and may involve fitting systematics, binning choices, and covariance between α and broadband nuisance terms in the monopole fit (Eq. 3.26).

Importantly, this shift is not mirrored by a corresponding quadrupole trend: the averaged quadrupole does not show a comparable systematic offset.

A more definitive interpretation would require multiple independent simulation realizations and a nuisance parameter covariance analysis, as is done in the DESI data release 2. [10]

5.2.1 Resolution

A practical limitation of the analysis is the finite separation binning used to measure $\xi(s, \mu)$ and the multipoles. With a typical bin width of $\Delta s = 3\,\mathrm{Mpc}$, sensitivity to small BAO peak shifts is limited: displacements significantly below this scale cannot be resolved and may be absorbed by broadband nuisance terms in Eq. 3.25. This limits the interpretation of cosmological parameters that have only a small impact on the Hubble parameter in Eq. 3.3. This could be a reason why the w_a constraints are poor within the 2 parameter (w_0, w_a) pipeline.

5.2.2 Volume

The FLAMINGO volume considered here is a periodic cube of side length $L = 1000\,\mathrm{Mpc}$ (Table 4.1), which limits the number of independent large scale modes available for BAO and hence causes the instability of high redshift measurements. [11] This is a key reason why w_a remains weakly constrained as introducing higher redshift bins such as $z = 0.9$ is not viable due to the low amount of tracers.

In contrast, DESI analyses rely on the AbacusSummit mock suite, which is based on dark matter only simulations with box sizes of up to $L = 2000\,h^{-1}$Mpc and an effective volume of approximately $(6\,h^{-1}\text{Gpc})^3$ achieved by tiling multiple realizations. This substantially increases the number of independent BAO-scale modes and allows for BAO measurements out to higher redshifts.[8, 10] Higher redshift measurements give you more constraints on (w_0, w_a) as that creates more linear combination of (w_0, w_a) in Eq. 3.4.

A further distinction lies in the galaxy halo connection model. In AbacusSummit, galaxies are populated into dark matter halos using a halo occupation distribution (HOD), which is calibrated to reproduce observed galaxy clustering and number densities but does not explicitly model baryonic physics.[9] In contrast, FLAMINGO is a fully hydrodynamical simulation in which galaxies form self-consistently from gas cooling, star formation, and feedback processes, without relying on an HOD prescription.[11] While this makes FLAMINGO particularly well suited for studying baryonic effects and galaxy formation physics, it comes at the cost of significantly reduced cosmological volume.

As can be seen from the results in table 4.2, the constraints on (w_0, w_a) from the `W0WA` and `W0WA+AGN` are practically the same. This may very well indicate that higher AGN feedback does not interfere with physics at BAO length scale.

5.3 Conclusion

In conclusion, BAO measurements extracted from FLAMINGO hydrodynamical simulations reproduce the expected BAO scale behaviour and yield w_0–w_a posteriors that deviate from ΛCDM in the direction expected for the underlying `W0WA` cosmology (Table 4.2; Figs. 4.7 and 4.10). The pipeline passes a key self-consistency check at $z = 0.5$ (Figs. 4.5 and 4.6), and the quadrupole diagnostic supports approximate isotropy near the true cosmology (Eq. 3.28). The dominant limitations arise from finite volume, reduced tracer density at higher redshift, and finite Δs resolution, which collectively hinder constraints on w_a and motivate the use of larger mock volumes for dark energy parameter inference, as adopted in the DESI analysis with AbacusSummit.[8, 10, 11]

Version of February 12, 2026– Created February 12, 2026 - 20:24

5.4 Outlook

Looking ahead, progress in constraining evolving dark energy with BAO will depend critically on extending both simulation volumes and observational redshift coverage. The present analysis demonstrates that BAO measurements extracted from hydrodynamical simulations are capable of recovering the correct BAO scale and responding in the expected direction to deviations from ΛCDM. However, the limited volume of FLAMINGO restricts the achievable signal-to-noise at higher redshift, where sensitivity to the time evolution of the dark energy equation of state becomes most pronounced.

Larger volume hydrodynamical simulations, with sizes of several $(\mathrm{Gpc})^3$, would enable stable BAO measurements at $z \gtrsim 1$ while retaining a self-consistent treatment of baryonic physics. Such simulations would significantly increase the number of independent BAO-scale modes and mitigate the low-tracer limitations encountered in the $z = 0.9$ shell of the present work. In this regime, multiple redshift bins could be combined to robustly sample the redshift evolution of $w(z)$, reducing degeneracies between w_0 and w_a and allowing meaningful constraints on dynamical dark energy without fixing either parameter beforehand.

On the observational side, upcoming DESI data releases will improve statistical precision through increased sky coverage, deeper exposures, and thus create larger number of well-populated redshift bins. As the survey approaches its full target volume, BAO measurements from LRGs, ELGs, and quasars will extend to $z \gtrsim 1.5$ up to $z \approx 4$, providing the redshift leverage required to break the (w_0, w_a) degeneracy.[9]

More broadly, very large volume dark matter only simulations, such as AbacusSummit, provide the most practical path forward for precision BAO cosmology. Their statistical power enables accurate covariance estimation and stable BAO measurements at high redshift. Fully hydrodynamical simulations, such as FLAMINGO, remain valuable for quantifying baryonic effects, but the results of this thesis support the conclusion that baryonic physics has a negligible impact on the BAO length scale relevant for cosmological inference. The added computational power required to run large volume hydrodynamical simulations is an extra downside of using FLAMINGO-like suites to create mock BAO measurements.

If future observations provide robust evidence for dynamically evolving dark energy, the implications would extend well beyond constraints on w_0 and w_a in itself. A departure from a cosmological constant would disfavour vacuum energy as the dominant explanation for cosmic acceleration and instead point toward dynamical degrees of freedom, such as scalar field models or modifications of gravity on large scales. In this scenario, measurements of the redshift evolution of the expansion history will be essential for discriminating between competing theoretical descriptions of dark energy and for clarifying whether cosmic acceleration arises from new physics or a breakdown of General Relativity on cosmological scales.

Version of February 12, 2026– Created February 12, 2026 - 20:24

Bibliography

[1] P. J. E. Peebles and J. T. Yu, *Primeval Adiabatic Perturbation in an Expanding Universe*, The Astrophysical Journal **162**, 815 (1970).

[2] C.-P. Ma and E. Bertschinger, *Cosmological Perturbation Theory in the Synchronous and Conformal Newtonian Gauges*, The Astrophysical Journal **455**, 7 (1995).

[3] D. J. Eisenstein and W. Hu, *Baryonic Features in the Matter Transfer Function*, The Astrophysical Journal **496**, 605 (1998).

[4] N. Aghanim et al., *Planck 2018 results: VI. Cosmological parameters*, Astronomy amp; Astrophysics **641**, A6 (2020).

[5] D. H. Weinberg, M. J. Mortonson, D. J. Eisenstein, C. Hirata, A. G. Riess, and E. Rozo, *Observational probes of cosmic acceleration*, Physics Reports **530**, 87â (2013).

[6] D. J. Eisenstein et al., *Detection of the Baryon Acoustic Peak in the LargeâScale Correlation Function of SDSS Luminous Red Galaxies*, The Astrophysical Journal **633**, 560â574 (2005).

[7] M. M. Ivanov, *Effective Field Theory for Large Scale Structure*, 2022.

[8] M. Abdul Karim et al., *DESI DR2 results. II. Measurements of baryon acoustic oscillations and cosmological constraints*, Physical Review D **112** (2025).

[9] D. Collaboration et al., *The DESI Experiment Part I: Science,Targeting, and Survey Design*, (2016).

Version of February 12, 2026– Created February 12, 2026 - 20:24

[10] U. Andrade et al., *Validation of the DESI DR2 measurements of baryon acoustic oscillations from galaxies and quasars*, Phys. Rev. D **112**, 083512 (2025).

[11] J. Schaye, R. Kugel, M. Schaller, J. C. Helly, J. Braspenning, W. Elbers, I. G. McCarthy, M. P. vanÂ Daalen, B. Vandenbroucke, C. S. Frenk, J. Kwan, J. Salcido, Y. M. BahÃ©, J. Borrow, E. Chaikin, O. Hahn, F. HuÅ¡ko, A. Jenkins, C. G. Lacey, and F. S. J. Nobels, *The FLAMINGO project: cosmological hydrodynamical simulations for large-scale structure and galaxy cluster surveys*, Monthly Notices of the Royal Astronomical Society **526**, 4978â5020 (2023).

[12] W. Hu and N. Sugiyama, *SmallâScale Cosmological Perturbations: An Analytic Approach*, The Astrophysical Journal **471**, 542 (1996).

[13] S. Angus, K. Cho, G. Franzmann, S. Mukohyama, and J.-H. Park,

$$\mathbf{O}(D, D)$$

completion of the Friedmann equations, The European Physical Journal C **80** (2020).

[14] S. Dodelson, *Modern Cosmology*, Academic Press, San Diego, 2003.

[15] A. Lewis, A. Challinor, and A. Lasenby, *Efficient computation of CMB anisotropies in closed FRW models*, **538**, 473 (2000).

[16] L. Senatore and M. Zaldarriaga, *The IR-resummed Effective Field Theory of Large Scale Structures*, Journal of Cosmology and Astroparticle Physics **2015**, 013â013 (2015).

[17] R. Panek, *The Most Shocking Discovery in Astrophysics Is 25 Years Old*, Scientific American (2023), Accessed: 2026-01-14.

[18] B. A. Bassett and R. Hlozek, *Baryon Acoustic Oscillations*, 2009.

[19] D. J. Eisenstein, H. Seo, and M. White, *On the Robustness of the Acoustic Scale in the LowâRedshift Clustering of Matter*, The Astrophysical Journal **664**, 660â674 (2007).

[20] C. Alcock and B. Paczyński, *An evolution free test for non-zero cosmological constant*, Nature **281**, 358 (1979).

[21] D. J. Eisenstein, H. Seo, E. Sirko, and D. N. Spergel, *Improving Cosmological Distance Measurements by Reconstruction of the Baryon Acoustic Peak*, The Astrophysical Journal **664**, 675â679 (2007).

[22] B. Ratra and P. J. E. Peebles, *Cosmological consequences of a rolling homogeneous scalar field*, Phys. Rev. D **37**, 3406 (1988).

[23] R. Caldwell, *A phantom menace? Cosmological consequences of a dark energy component with super-negative equation of state*, Physics Letters B **545**, 23â29 (2002).

[24] A. Vikman, *Can dark energy evolve to the phantom?*, Physical Review D **71** (2005).

[25] Y. Gong, Q. Gao, and Z.-H. Zhu, *The effect of different observational data on the constraints of cosmological parameters*, Monthly Notices of the Royal Astronomical Society **430**, 3142 (2013).

[26] R. Calderon et al., *DESI 2024: reconstructing dark energy using crossing statistics with DESI DR1 BAO data*, Journal of Cosmology and Astroparticle Physics **2024**, 048 (2024).

[27] T. M. C. Abbott et al., *Dark Energy Survey Year 3 results: Constraints on extensions to ΛCDM with weak lensing and galaxy clustering*, Phys. Rev. D **107**, 083504 (2023).

[28] C. Blake, S. Brough, M. Colless, C. Contreras, W. Couch, S. Croom, D. Croton, T. Davis, M. Drinkwater, K. Forster, D. Gilbank, M. Gladders, K. Glazebrook, B. Jelliffe, R. Jurek, I.-h. Li, B. Madore, C. Martin, K. Pimbblet, and H. Yee, *The WiggleZ Dark Energy Survey: Joint measurements of the expansion and growth history at $z < 1$*, Monthly Notices of the Royal Astronomical Society **425** (2012).

[29] R. Zhou et al., *Target Selection and Validation of DESI Luminous Red Galaxies*, The Astronomical Journal **165**, 58 (2023).

[30] R. Kennedy, S. P. Bamford, I. Baldry, B. HÃ€uÃler, B. W. Holwerda, A. M. Hopkins, L. S. Kelvin, R. Lange, A. J. Moffett, C. C. Popescu, E. N. Taylor, R. J. Tuffs, M. Vika, and B. Vulcani, *Galaxy And Mass Assembly (GAMA): the wavelength dependence of galaxy structure versus redshift and luminosity*, Monthly Notices of the Royal Astronomical Society **454**, 806â817 (2015).

[31] J. Bagchi, S. Sankhyayan, P. Sarkar, S. Raychaudhury, J. Jacob, and P. Dabhade, *Saraswati: An Extremely Massive âŒ200 Megaparsec Scale Supercluster*, The Astrophysical Journal **844**, 25 (2017).

[32] M. Sinha and L. Garrison, *CORRFUNC: Blazing Fast Correlation Functions with AVX512F SIMD Intrinsics*, in *Software Challenges to Exascale Computing*, edited by A. Majumdar and R. Arora, pages 3–20, Singapore, 2019, Springer Singapore.

[33] M. Sinha and L. H. Garrison, *CORRFUNC - a suite of blazing fast correlation functions on the CPU*, **491**, 3022 (2020).

[34] S. D. Landy and A. S. Szalay, *Bias and Variance of Angular Correlation Functions*, **412**, 64 (1993).

[35] A. J. S. Hamilton, *Measuring Omega and the Real Correlation Function from the Redshift Correlation Function*, **385**, L5 (1992).

[36] P. Norberg, C. M. Baugh, E. Gaztañaga, and D. J. Croton, *Statistical analysis of galaxy surveys - I. Robust error estimation for two-point clustering statistics*, **396**, 19 (2009).

[37] K. M. Gorski, E. Hivon, A. J. Banday, B. D. Wandelt, F. K. Hansen, M. Reinecke, and M. Bartelmann, *HEALPix: A Framework for High-âResolution Discretization and Fast Analysis of Data Distributed on the Sphere*, The Astrophysical Journal **622**, 759â771 (2005).

[38] W. Fang, W. Hu, and A. Lewis, *Crossing the phantom divide with parametrized post-Friedmann dark energy*, Phys. Rev. D **78**, 087303 (2008).

[39] X. Xu, A. J. Cuesta, N. Padmanabhan, D. J. Eisenstein, and C. K. McBride, *Measuring D_A and H at z=0.35 from the SDSS DR7 LRGs using baryon acoustic oscillations*, **431**, 2834 (2013).

[40] L. Anderson et al., *The clustering of galaxies in the SDSS-III Baryon Oscillation Spectroscopic Survey: baryon acoustic oscillations in the Data Releases 10 and 11 Galaxy samples*, Monthly Notices of the Royal Astronomical Society **441**, 24â62 (2014).

[41] N. Kaiser, *Clustering in real space and in redshift space*, Monthly Notices of the Royal Astronomical Society **227**, 1 (1987).

[42] J. Hartlap, P. Simon, and P. Schneider, *Why your model parameter confidences might be too optimistic. Unbiased estimation of the inverse covariance matrix*, Astronomy amp; Astrophysics **464**, 399â404 (2006).

[43] S. Alam et al., *The clustering of galaxies in the completed SDSS-III Baryon Oscillation Spectroscopic Survey: cosmological analysis of the DR12 galaxy sample*, Monthly Notices of the Royal Astronomical Society **470**, 2617â2652 (2017).

[44] L. C. Kimmig, R.-S. Remus, B. Seidel, L. M. Valenzuela, K. Dolag, and A. Burkert, *Blowing Out the Candle: How to Quench Galaxies at High RedshiftâAn Ensemble of Rapid Starbursts, AGN Feedback, and Environment*, The Astrophysical Journal **979**, 15 (2025).

[45] J. S. Speagle, *A Conceptual Introduction to Markov Chain Monte Carlo Methods*, 2020.